

IN-PLANE STRESS ANALYSIS USING TENSOR FIELD
PHOTOELASTICITY

by

Sui Gao

B.A.Sc., University of Waterloo, 2009

A THESIS SUBMITTED IN PARTIAL FULFILLMENT OF
THE REQUIREMENTS FOR THE DEGREE OF

MASTER OF APPLIED SCIENCE

in

THE FACULTY OF GRADUATE STUDIES

(Mechanical Engineering)

THE UNIVERSITY OF BRITISH COLUMBIA

(Vancouver)

August 2011

© Sui Gao, 2011

Abstract

Few experimental methods exist for evaluating all in-plane stress components in solid materials; because of the tensor nature of these quantities. Full field measurement of all three stress components is desirable, since plastic deformation or failure can result from any combination of the three. A new photoelastic stress measurement method is presented for evaluating all three in-plane stress components within a two-dimensional photoelastic material. The measurement method is based on the observation that the complex transmission factors that describe the optical phase changes due to stress-induced birefringence have a second order tensor character, similar to that of other tensor quantities such as stress and strain. The same transformation equations and Mohr's circle construction can be applied to the rotation of optical axis. A Michelson type interferometer and phase shifting are used to quantify the phases of the complex transmission factors. Mohr's circle calculation is applied to obtain the principal transmission factors and principal axis orientation. The principal stresses are then obtained from the principal transmission factors through the stress optical relationship. The effectiveness of this technique is demonstrated by comparing the experimental and analytical results for a hollow circular ring under diametric compression.

Table of Contents

Abstract	ii
Table of Contents	iii
List of Figures	v
Nomenclature	viii
Acknowledgements	x
Chapter 1 – Introduction	1
1.1 Experimental Stress Analysis	1
1.1.1 Motivation	2
1.2 In-Plane Stress Measurement Methods	2
1.2.1 Strain Gauges	3
1.2.2 Thermoelasticity	4
1.2.3 Optical Displacement Measurement Methods	5
1.2.4 Photoelasticity	6
1.2.4.1 Classical Photoelasticity	7
1.2.4.2 Interferometric Photoelasticity	8
1.2.4.3 Photoelastic Stress Separation	9
1.3 Research Objective and Proposed Method	10
Chapter 2 – Theoretical Background	13
2.1 Introduction to Polarization of Light and Birefringence	13
2.2 In-Plane Stress	15
2.3 Stress Optical Relationship	17
2.4 Tensor Field Character of Birefringence	22
2.5 Phase Stepping Interferometry	26
2.6 Far Field Drift Compensation	29
Chapter 3 – Modifications to Interferometric Photoelastic Measurement Method	31
3.1 Introduction to Interferometric Photoelasticity	31
3.2 Proposed Experiment Configuration	32

3.2.1 Secondary Beam Expansion	33
3.2.2 Optical Phase Detection	36
3.2.3 Phase Shifting Implementation	37
3.2.4 Polarization Control	41
3.3 Tuning and Adjustment.....	42
3.4 Experiment Challenges and Solution.....	46
Chapter 4 – Experimental Validation	50
4.1 Experiment Overview	50
4.2 Photoelastic Test Specimen	50
4.3 Polarized Phase Measurement of Birefringence	53
4.4 Calculation of Principal Transmission Factors	55
4.5 Stress Optical Coefficient Evaluation	56
4.6 Stress Distribution Comparison	57
Chapter 5 – Discussions	62
5.1 Comparison with Classical Photoelastic Method	62
5.2 Improvements to Current Measurement Method.....	64
5.3 Future Work and Applications.....	66
Chapter 6 – Conclusions.....	70
6.1 Research Summary and Contributions.....	70
6.2 Comparison with other in-plane stress measurement methods.....	71
References.....	74

List of Figures

Figure 1 – Strain Gauge.....	3
Figure 2 – Thermoelastic Experiment Setup.....	4
Figure 3 – Digital Image Correlation.....	5
Figure 4 – Photoelastic Induced Optical Birefringence.....	7
Figure 5 – Photoelastic Fringe Pattern in Polariscope.....	8
Figure 6 – Interferometric Photoelastic Optical Configuration.....	9
Figure 7 – Horizontally Polarized Illumination of Birefringent Material.....	11
Figure 8 – Optical Tensor Axis Rotation.....	12
Figure 9 – Electromagnetic Wave of Plane Polarized Light.....	13
Figure 10 – Electromagnetic Wave of Elliptically Polarized Light.....	14
Figure 11 – Optical Transmission Through Wave Plate.....	15
Figure 12 – General State of Plane Stress.....	16
Figure 13 – Observation Axis Rotation of Plane Stress.....	17
Figure 14 – Stress Optical Relationship.....	18
Figure 15 – Plane Stress Poisson’s Effect.....	19
Figure 16 – Polarization Measurement of Photoelastic Material.....	23
Figure 17 – Mohr’s Circle Relationship of Complex Transmission Factors.....	24
Figure 18 – Superposition of Electromagnetic Fields.....	26
Figure 19 – Phase Stepping Algorithm.....	28
Figure 20 – Drift compensation by far field phase subtraction.....	30
Figure 21 – Optical Layout of Interferometer.....	33
Figure 22 – Experiment optical equipment.....	33

Figure 23 – Ray Diagram of Laser Beam Expansion.....	34
Figure 24 – Ray Diagram of Second Stage Beam Expander.....	35
Figure 25 – Double Image Due to Collimation Lens Misalignment.....	36
Figure 26 – Ray Diagram of Camera Lens.....	37
Figure 27 – Piezo-Electric Actuated Mirror.....	38
Figure 28 – Phase Shifted Measurement Images.....	39
Figure 29 – Computed Phase Map.....	40
Figure 30 – Far Field Drift Subtraction.....	40
Figure 31 – Plane Polarizing Filter and Attenuator.....	41
Figure 32 – Final Adjusted Two Beam Interference.....	42
Figure 33 – Interference of Two Oblique Plane Waves.....	45
Figure 34 – Beamsplitter Placement.....	46
Figure 35 – Static Deformation of Optical Table Due to Compression.....	47
Figure 36 – Deformation Compensation by Preloading.....	48
Figure 37 – Circular Ring Specimen under Compression.....	50
Figure 38 – Photograph of Test Specimen and Loading Apparatus.....	53
Figure 39 – Polarized Phase Measurements.....	54
Figure 40 – Calculated Principal Components of Birefringence.....	56
Figure 41 – Cross Section Phase Comparison of C3.....	57
Figure 42 – In-Plane Stress Distribution Comparison.....	59
Figure 43 – Measured and Analytical Stress Profiles Along a Horizontal Line a Quarter Diameter Below the Upper Contact Point.....	60
Figure 44 – Classical Photoelasticity Optical Arrangement.....	62

Figure 45 – Classical Photoelastic Fringe Observation	64
Figure 46 – Phase Disturbance From Polarizer Movement.....	65
Figure 47 – Surface Strain Measurement Using Reflection Photoelasticity	67
Figure 48 – Applying Tensor Field Measurement to Reflection Photoelasticity	68

Nomenclature

Symbol	Description	SI Units
A, B	Maxwell Neumann stress optical coefficients	m^2/N
A', B'	Final stress optical coefficients	m^2/N
C1, C2, C3, C4	Directional transmission factors	Complex unitless
F	Force	N
h	Thickness of unstressed specimen	m
h'	Thickness of stressed specimen	m
Δh	Change in specimen thickness due to loading	m
F	Applied force	N
G	Average intensity of phase shifting	W/m^2
H	Modulation intensity of phase shifting	W/m^2
E	Young's modulus	N/m^2
I₁, I₂, ... I₈	Pixel intensities	N/m^2
n₀	Refractive index of air	
n	Refractive index of unstressed photoelastic specimen	
p, q, t	isotropic and deviatoric components of the transmission factors	Complex unitless
n₁, n₂	Polarized refractive indices of stressed photoelastic specimen	
U_{in}, U_{out}	Electric field entering and exiting an unstressed specimen	V/m
U'_{in}, U'_{out}	Electric field entering stressed specimen	V/m
U_x, U_y	Electric fields of horizontal and vertical polarization components	V/m

Symbol	Description	SI Units
U_a, U_b	Electric field of two light beams	V/m
u, v	Principal transmission factors	Complex unitless
α	Phase drift due to change in air pressure	radians
β_n	Phase shifting value (piezo position)	radians
σ_1, σ_2	Principal stresses	N/m^2 (Pa)
$\sigma_x, \sigma_y, \tau_{xy}$	In-plane stresses in Cartesian coordinates	N/m^2 (Pa)
$\sigma_r, \sigma_\theta, \tau_{r\theta}$	In-plane stresses in radial coordinates	N/m^2 (Pa)
$\varepsilon_x, \varepsilon_y, \varepsilon_{xy}$	In-plane strains in Cartesian coordinates	m/m
ε_z	Out-of-plane strains in Cartesian coordinates	m/m
Φ_1, Φ_2	Phase change across unstressed specimen	radians
Φ'_1, Φ'_2	Phase changes across stressed specimen	radians
φ_1, φ_2	Phase change due to applied stress	radians
φ_a, φ_b	Optical phase of two light beams	radians
λ	Wavelength of monochromatic light (532nm)	m
ν	Poisson's ratio	
θ	Principal angle for optical and principal stress axes	radians

Acknowledgements

I first want to sincerely thank my supervisor Dr. Gary Schajer for his mentorship and guidance throughout my research at UBC. Secondly all the staffs in the department of Mechanical Engineering have been very supportive. And finally I dedicate my thesis to my parents for their love and support.

Chapter 1 – Introduction

1.1 Experimental Stress Analysis

Experimental stress analysis provides important means of evaluating mechanical stresses in solid materials. In comparison with other stress analysis methods such as analytical stress analysis and numerical solutions, experimental stress analysis does not rely on modelling of the material of interest and the associated loads and boundary conditions for evaluating the stress distribution. However, it can often be difficult to evaluate stresses experimentally because of the tensor nature of stresses and their location within materials [1].

Currently, industry practice relies heavily on numerical solutions such as Finite Element Analysis (FEA). One crucial drawback of using numerical solutions such as FEA is that the solution is highly dependent on loading and boundary conditions, which at times can be difficult to determine reliably [2][3]. Experimental stress analysis overcomes this drawback, since the boundary and loading conditions in experiments are themselves real and therefore can be used to verify FEA results.

The main focus in the field of experimental stress analysis is the development of methods or combination of methods where more information about stresses and/or deformations in materials can be extracted. Incomplete stress distribution measurements can only partially verify numerical solutions. Improvements in stress measurement methods can thus provide engineers and designers with greater confidence and quality in their design of components and structures.

1.1.1 Motivation

Photoelasticity is a well established method of experimentally determining stress distributions. One of the main challenges of using such method has been its difficulty in determining all stress components. In the case of determining in-plane stresses in flat materials of uniform thickness, the classical photoelastic method can only determine two of the three stress components, and therefore provides an incomplete solution. A new measurement method is thus needed to determine all three stress components. From an engineering perspective, the new method should retain the convenient operations of the classical method as much as possible, while providing repeatable and accurate measurements.

1.2 In-Plane Stress Measurement Methods

The tensor nature of plane stress fields makes them particularly difficult to evaluate. Full field measurement of all three components of plane stress components is necessary, since plastic deformation or failure can result from any combination of the three stress components. All measurement methods rely on measuring either strain or displacement, from which the corresponding stresses are inferred. Some measurement methods provide point-wise data while other can provide full-field measurements, i.e., many measurements spread over an extended area. However, most methods of either kind provide specific strain or stress components, typically not all of them.

1.2.1 Strain Gauges

Strain gauges are devices bonded to a surface of interest for measuring surface strains in specific directions, as below shown in figure 1. These devices rely on changes in their electrical resistance in response to their elongation or compression. A strain gauge is firmly bonded to the material specimen so that it shares the same local surface deformations. The elongation and compression of the conductive wires inside strain gauges alter their electrical resistance. This change can then be measured and translated to the strain of the electric wires.

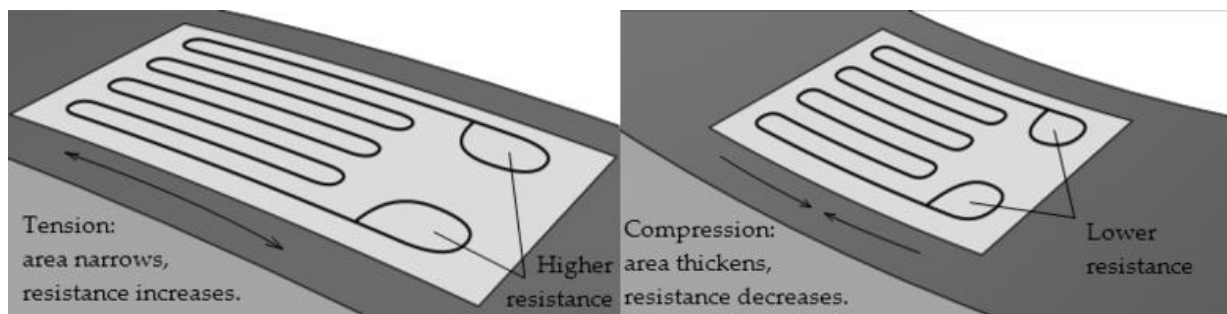


Figure 1: Strain Gauge

Strain gauges are very sensitive and accurate devices. A precisely calibrated strain gauge can achieve resolution in the micro-strain range, and micrometer displacement accuracy [4]. Signal conditioning makes them resistant to environment disturbances such as temperature drifts. The main limitation in conducting in-plane stress analysis using strain gauges is that they only provide point-wise measurements. Without full-field measurement, areas of high stress concentrations on the surface can be unnoticed. In addition, strain gauges measure strains in single directions, thus multiple strain gauges must be used if measurements in multiple directions are required.

1.2.2 Thermoelasticity

Thermoelastic stress analysis relies on thermal imaging cameras to detect thermal energy changes within a material when stress is applied. The change in thermal energy is due to change in the intermolecular spacing of the material. During compression, the intermolecular spacing is reduced, causing increased vibration of the atoms or molecules and thus increasing the local temperature. The reverse occurs when the material is in tension, and local temperature is reduced. Figure 2 shows a metal plate under compression imaged by a thermal imaging camera.

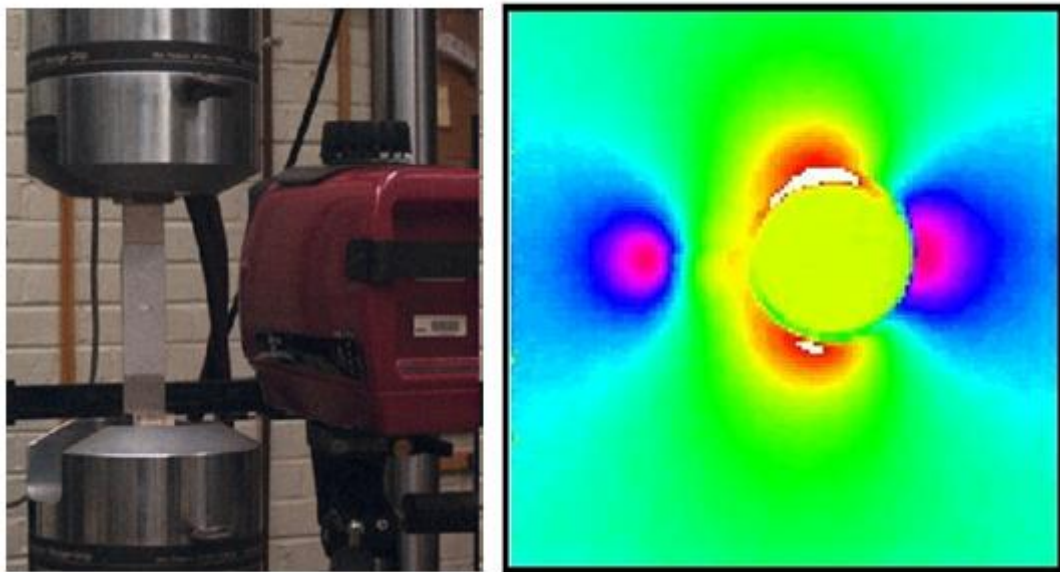


Figure 2: Thermoelastic Experiment Setup

Thermoelasticity provides full field measurements, and is well suited for application where dynamic load is applied. In vibration measurements for example, areas of the material where deformation occurs at high frequencies give off high thermal energy. [5] In static loading applications, thermoelastic measurement can only translate to the sum of the principal

stresses, which is only one of the three in-plane stress components. Moreover, most materials have a thermoelastic coefficient of between $-0.44 \times 10^{-3} \text{ } \epsilon/\Delta T$ and $0.33 \times 10^{-3} \text{ } \epsilon/\Delta T$ [6] and even when with modern thermal imaging cameras, sensitivity is in the milli-strain range.

1.2.3 Optical Displacement Measurement Methods

Optical displacement measurement methods such as Digital Image Correlation (DIC) employ image processing techniques to track changes to an object viewed from a digital camera, as illustrated in figure 3. Markers are used on an object or surface of interest to calculate the displacement and strain induced during deformation. DIC has proven to be effective at mapping both normal and shear strains simultaneously [7]. Even with sub-pixel interpolation techniques, DIC has low strain resolution. Typical applications of DIC are made on highly elastic materials such as plastics, where strains are large.

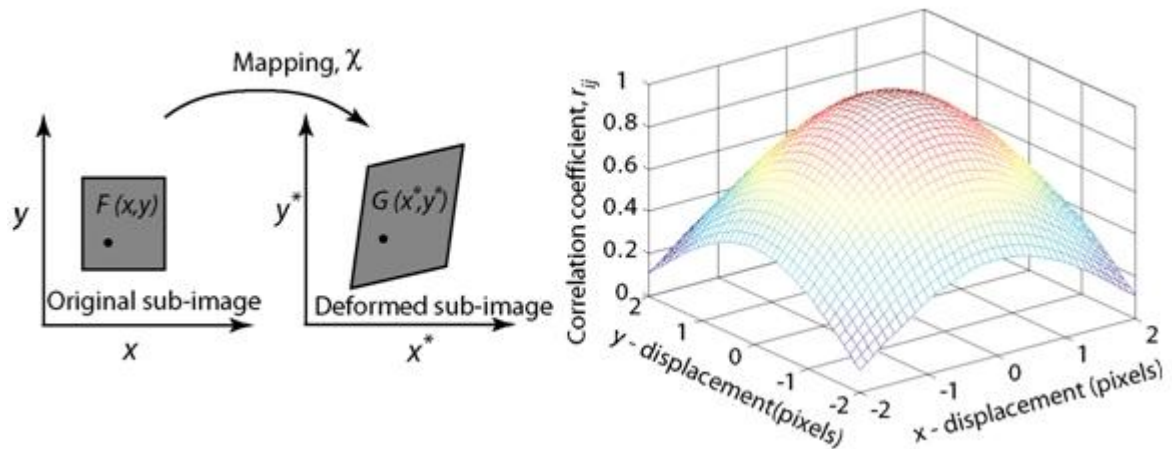


Figure 3: Digital Image Correlation

High resolution optical testing techniques such as Electronic Speckle Pattern Interferometry (ESPI) can also be used for full field measurement of stress and strain. This

technique works by creating an interference pattern from two light sources of the same wavelengths: one from an expanded laser source and another from the scattered light off an optically rough surface. Displacement changes on the optically flat surface alter the optical path difference between the two light sources, resulting in a change in interference pattern. The interference nature of light used in ESPI signifies that the displacement resolution is in the nanometre range, and a full sensing range of a few microns with the aid of phase unwrapping [8]. The main limitation in using ESPI to measure in-plane stress/strain is that the measurements are scalars as oppose to tensor quantities in stresses. Different ESPI configurations can be used to measure displacement in-plane or out-of-plane, depending on where the interference takes place.

1.2.4 Photoelasticity

Photoelasticity is a non-contact and full-field measurement method for analyzing stress distributions in transparent materials such as glass and plastic. This method is based on the property of optical birefringence in certain transparent materials. As illustrated in figure 4, when stress is induced in these materials, their tensor refractive index alters and causes the two polarization components of light pass through to experience relative phase retardation (difference in phase between the two polarization components of light existing the material).

Two-dimensional photoelasticity involves photoelastic materials of uniform thickness, where stress is uniform in the normal direction of plane deformation. In this loading condition, there is no rotation of principal axis within the material and the stress optical relationship is linear [9].

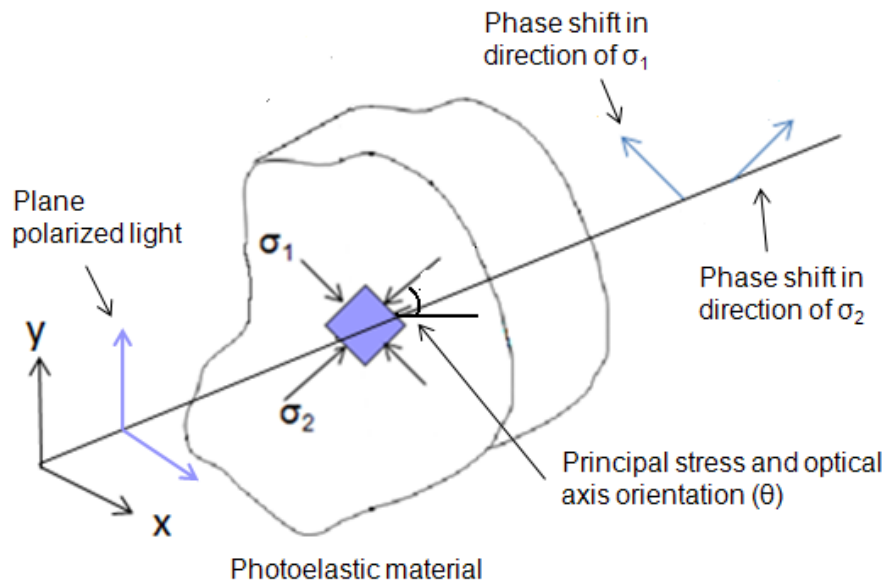


Figure 4: Photoelastic Induced Optical Birefringence

1.2.4.1 Classical Photoelasticity

Classical photoelasticity measurements consist of monochromatic light passing through photoelastic material under stress placed between two polarizing filters. The observed fringe pattern yields solutions to the principal stress differences (Isochromatics) and principal angles (isoclinics): that the optical birefringence effect creates a relative phase difference (retardation) between the two polarization components of light oscillating parallel to the principal stress directions, and the polarizing filters allow this effect to be observed. [10] Figure 5 shows a rectangular specimen under four-point compression placed between two polarizing filters oriented parallel to one another. The shear stresses caused by the bending moment produce evenly spaced stress fringes in the specimen. High stress concentrations are located at the contact points on the specimen. The birefringence effect is wavelength dependent, resulting in separation of the multi-wavelength components of white light.

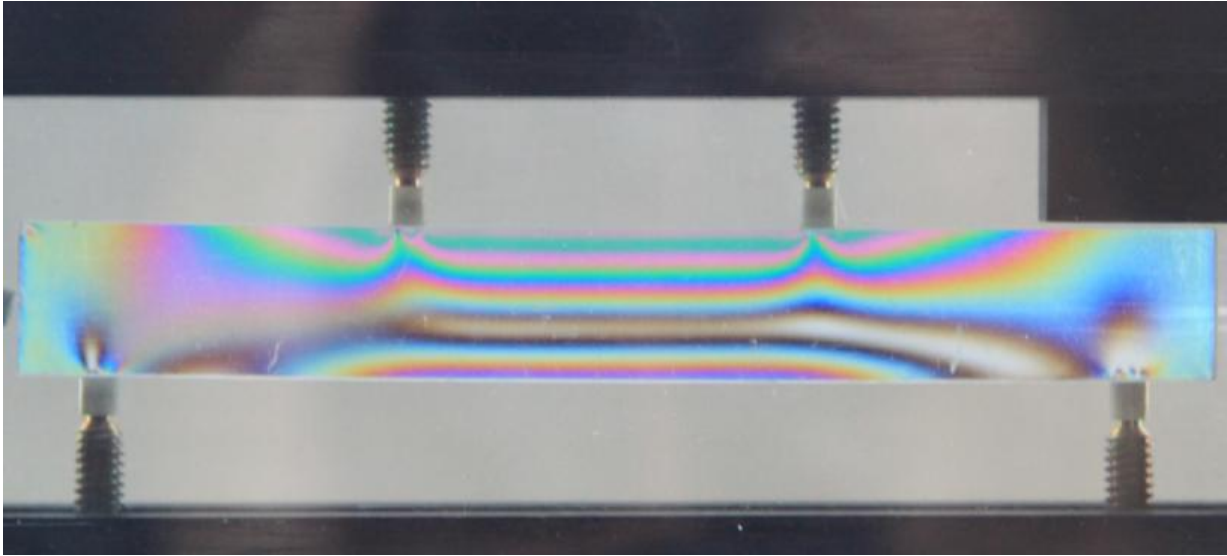


Figure 5: Photoelastic Fringe Pattern in Polariscope

1.2.4.2 Interferometric Photoelasticity

Interferometric photoelasticity allows measurements of absolute variations in optical phase, as oppose to the relative phase retardation in classical photoelasticity. The measurement of absolute changes in optical phase offers the possibility of evaluating all in-plane stress components. The experiment setup consists of placing a photoelastic specimen in a Mach-Zehnder as shown in figure 6. Existing work relies on interpreting interference fringes and analyzing optical intensity measurements as oppose to optical phase measurements. The main challenge in interpreting intensity measurements is that they are nonlinear function of principal stress differences and principal stress sums, making stress separation difficult. [11] Another drawback of analyzing intensity instead of phase is that the interference patterns do not yield solution to the principal angle orientation. [12]

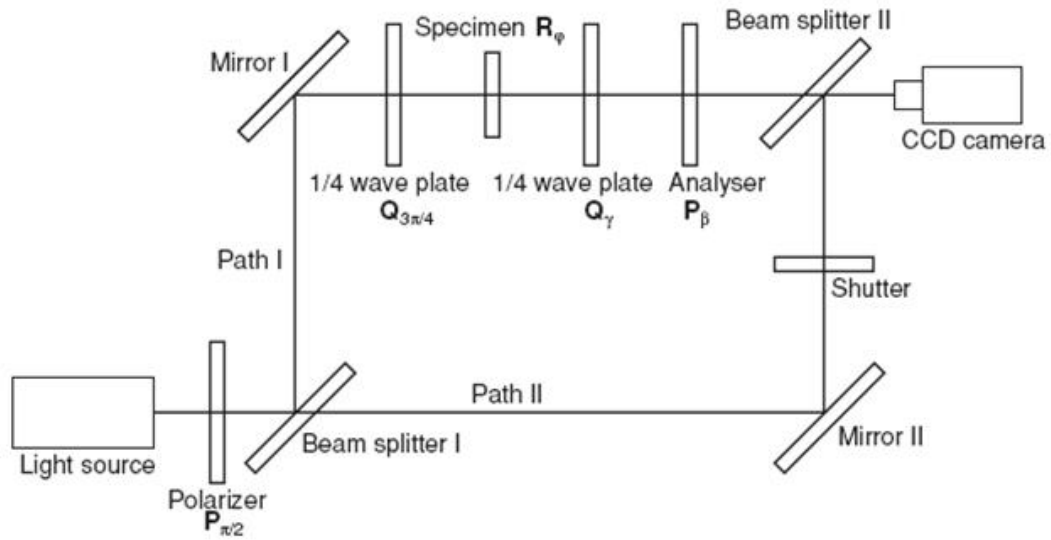


Figure 6: Interferometric Photoelastic Optical Configuration

1.2.4.3 Photoelastic Stress Separation

Because methods like classical and intensity measurements from interferometric photoelasticity do not provide all in-plane stress components, many hybrid methods have been proposed that involve combining two or more sets of different methods for all in-plane stress components. For example, thermoelasticity can only measure principal stress sums, while classical photoelastic method can measure principal stress differences and principal angle. [10] Others include numerical methods of applying equilibrium conditions to photoelastic measurements. [5] Combining classical photoelastic measurements with interferometric photoelastic measurements have shown to be the most attractive, due to their similar experiment equipment needs and independence from numerical calculation errors. Separation of the principal stress differences, sums and principal angle by combining classical photoelastic measurements with interferometric photoelastic intensity measurements has been proposed in

1964 [12] and recently demonstrated in 2005 [13]. Much of the challenge in this approach is that the intensity measurements are nonlinear functions of these stress components.

1.3 Research Objective and Proposed Method

A new measurement method is proposed for the measurement of plane stresses by directly measuring the phase changes of birefringence using phase shifting interferometry. This method is comparable to the interferometric photoelastic method, because of the similarities in equipments used. The key difference is that the discussed method relies on interpreting intensity measurements to solve non-linear relationships of the stress components, and the new method directly measures optical phase and treats the birefringence as a tensor quality, in which the optical stress relationships are linear. This new method offers the possibility of simplifying the number of measurements needed to extract the in-plane stress components.

Tensor field quantities are normally associated with mechanical quantities such as stress, strain, and moments/products of inertia [14]. They can also be used to mathematically represent the effect of electromagnetic wave propagating in orthotropic medium. [15] Representing birefringence as a tensor quantity has the advantage of utilizing existing mathematical tools such as Mohr's circle for processing these quantities. The birefringence tensor field can be characterized by two principal transmission factors and an axis orientation angle much like other second order tensor quantities such as mechanical stress. The transmission factors are mathematically complex values that characterize optical attenuation and phase changes. The optical behaviour of polarized light travelling in the birefringence tensor field can be mathematically predicted based on the Mohr's circle relationship, shown in figure 7 and 8. The principal transmission factors that correlate with the principal stresses at a

given point form the horizontal edges of Mohr's circle. The location of any given point on the circle is related by the axis angle: Rotation of the polarization angle of illumination effectively rotates the observation angle of the optical tensor. The resultant depolarization effect and phase change of in-plane polarization can then be predicted according to this relationship.

The purpose of this research is to explore the extent in which the tensor quality of birefringence can be used for measuring in plane stresses in photoelastic materials of uniform thicknesses. By taking a number of polarized phase measurements of a specimen before and after loading, an optical tensor field can be constructed. Applying the same transformation equations and Mohr's Circle construction as mechanical stress tensor fields, principal optical axes orientations and phase changes along principal optical axes can be determined. Principal stress orientation corresponds with optical stress orientation, and principal stresses are linear combinations of phase changes along the principal axes.

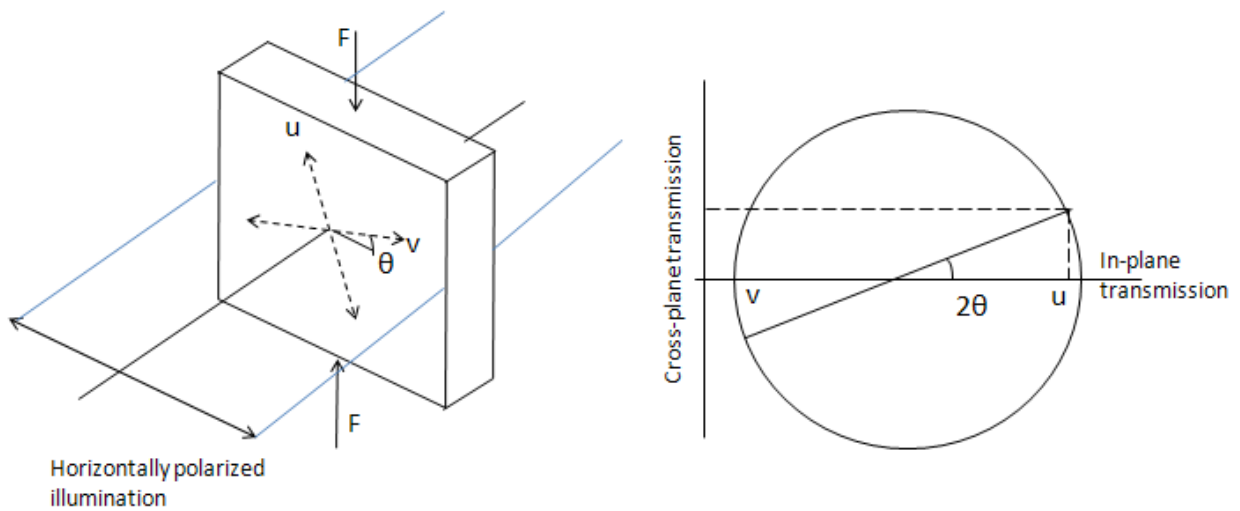


Figure 7: Horizontally Polarized Illumination of Birefringent Material

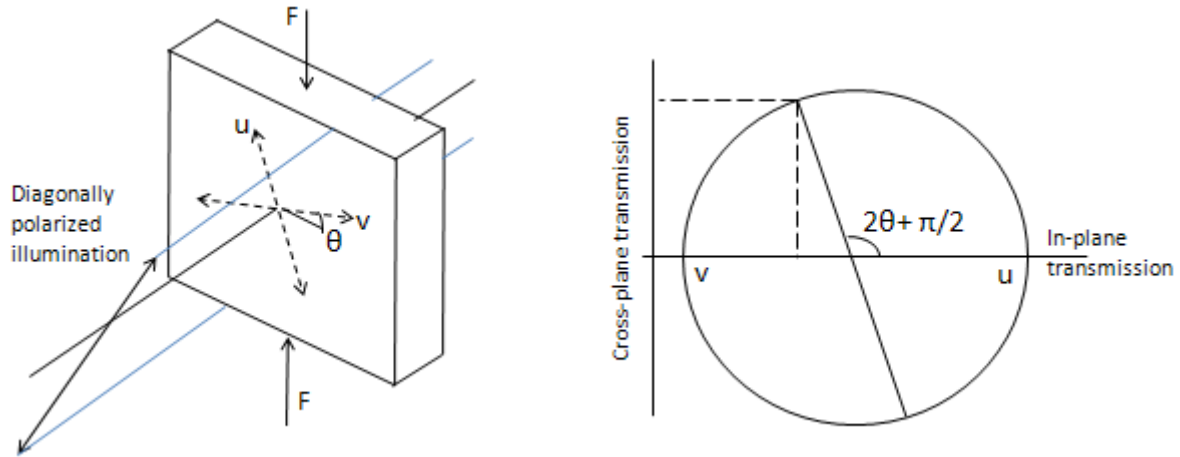


Figure 8: Optical Tensor Axis Rotation

The research objective is to explore the practicality of the proposed method. A new Michelson type interferometer design with improved sensitivity and larger field of view is used to conduct experiments. Phase shifting is used to quantify the optical phase changes, and polarization filters are used to separate specific polarization components of the birefringence. The effectiveness of the proposed technique can be demonstrated by measuring photoelastic specimens of a known stress distribution and compared the experimental results with the theoretical solution.

2 Theoretical Background

2.1 Introduction to Polarization of Light and Birefringence

Plane polarized light is an electromagnetic wave propagating axially. The plane of the polarization can be in any given angle when viewed along the propagation direction.

Typically, the wave is resolved into two mutually perpendicular polarization components. The features of monochromatic coherent light, i.e., light that consists of single frequency and a uniform wave-front, can be mathematically expressed using Jones Calculus. The general Jones vector expresses the two polarization components of the electromagnetic field of light in terms of two independent complex amplitudes, each consisting of a magnitude and a phase (equation 1). Due to the monochromatic nature of light considered, the time dependency is neglected in Jones Calculus [16].

$$\begin{bmatrix} U_x \\ U_y \end{bmatrix} = \begin{bmatrix} |U_x| e^{i\phi_x} \\ |U_y| e^{i\phi_y} \end{bmatrix} \quad (1)$$

Equation 1 can be visualized in Figure 9, where U_x and U_y are the complex fields of the polarization components. Φ_x and Φ_y are the phases of the fields at given point in space.

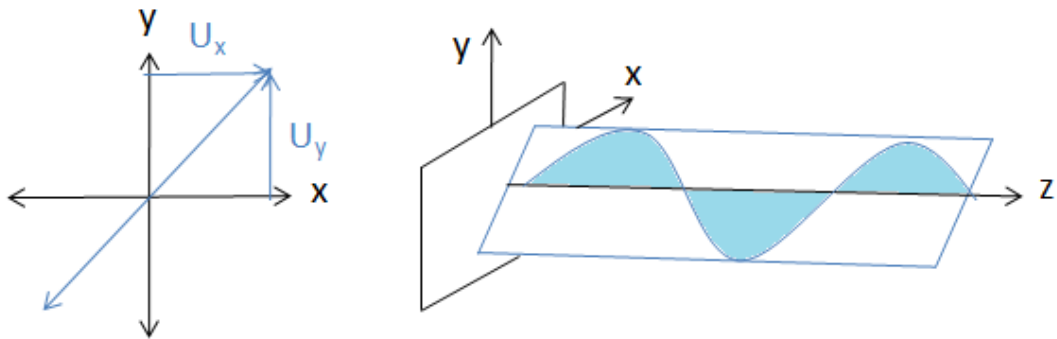


Figure 9: Electromagnetic Wave of Plane Polarized Light (see [16] for more details)

In the case of plane polarized light, the amplitudes U_x and U_y are the directional sine and cosine components of the wave. The phases Φ_x and Φ_y are coincident because of the plane wave nature. While in the case of elliptical polarized light in figure 10 below, the phases of the polarization components are 90° displaced.

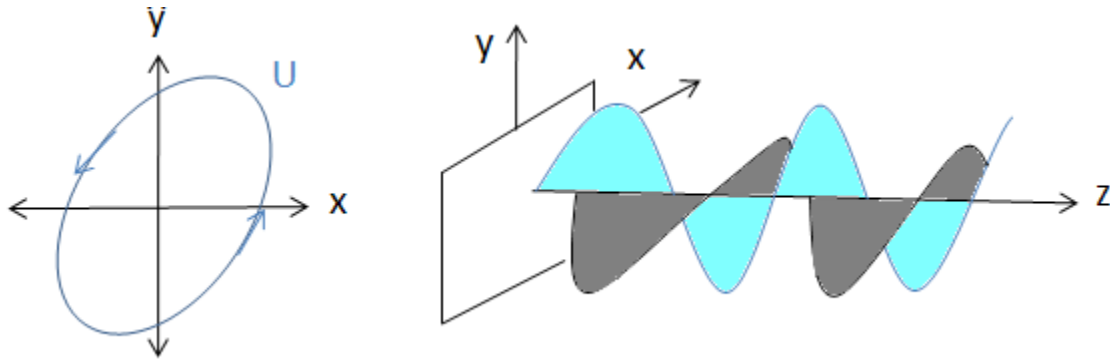


Figure 10: Electromagnetic Wave of Elliptically Polarized Light

Changes in the characteristics of polarized light propagating through different optical media can be mathematically expressed using a Jones matrix. This second order matrix characterizes amplitude and phase changes for each of the two polarization components of the Jones vector. An example is a phase retarder or wave plate. These components have different refractive

$$\begin{bmatrix} U_x \\ U_y \end{bmatrix}_{\text{out}} = \begin{bmatrix} e^{i\phi_x} & 0 \\ 0 & e^{i\phi_y} \end{bmatrix} \begin{bmatrix} U_x \\ U_y \end{bmatrix}_{\text{in}} \quad (2)$$

indices depending on the polarization of light passing through. As illustrated in figure 11, light polarized in the y' axis has a lower refractive index than in the x' axis. The y' and x' axis are referred to as fast and slow axis respectively; the lower refractive index in the y' axis causes the y' polarization component of the beam to speed up relative to the x' component. The difference in refractive index introduces a phase shift between the vertical and horizontal component of the field and thus change the polarization of the beam. The corresponding Jones

matrix for the phase retarder is expressed in equation 2. Amplitude and depolarization changes are neglected from the assumption of losses transmission.

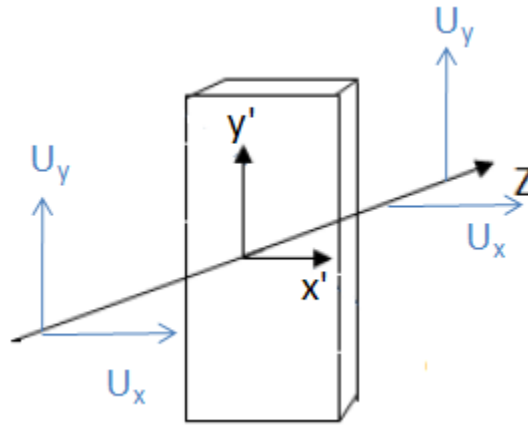


Figure 11: Optical Transmission Through Wave Plate

2.2 In-Plane Stress

In many practical cases, elastic deformation can be treated as being two dimensional. In these situations, deformation occurs primarily within a single plane of the material, while little action occurs in the normal direction. A typical example would be the membrane stresses within a thin plate. The general plane stress and strain tensors for any point in a material can be illustrated in Figure 12 and mathematically expressed as the following:

$$\sigma = \begin{bmatrix} \sigma_x & \tau_{xy} & 0 \\ \tau_{yx} & \sigma_y & 0 \\ 0 & 0 & 0 \end{bmatrix} \quad \varepsilon = \begin{bmatrix} \varepsilon_x & \varepsilon_{xy} & 0 \\ \varepsilon_{yx} & \varepsilon_y & 0 \\ 0 & 0 & \varepsilon_z \end{bmatrix} \quad (3)$$

where σ_x and σ_y are the normal stresses acting in the x and y directions, and τ_{xy} and τ_{yx} are the associated shear stresses. The corresponding strain tensor is similar, where the stress and strain/deformation is linearly related by Young's modulus (E) and Poisson's ratio (ν). [17]

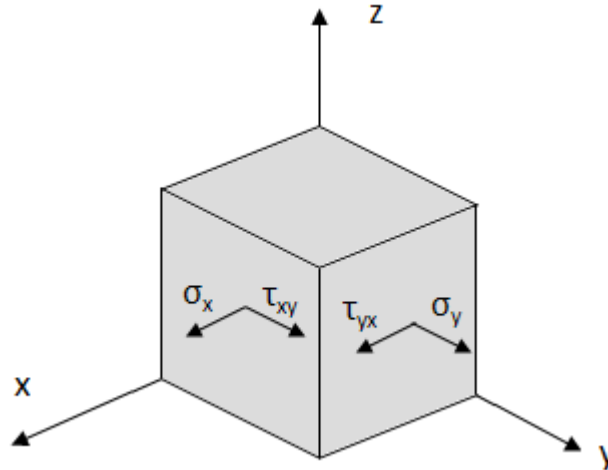


Figure 12: General State of Plane Stress

This is illustrated in Figure 13. For every point, there is an observation angle in which the shear stresses are zero; in this case, the normal stresses are referred to as principal stresses (σ_1 and σ_2), and the angle of observation with respect to the reference (x, y) axis is referred to as principal angle (θ). The three components of plane stress can then be defined as principal stresses and principal angle. Alternatively, plane stresses can also be defined as sum and difference of principal stresses $\sigma_1 + \sigma_2$ and $\sigma_1 - \sigma_2$.

$$\sigma = \begin{bmatrix} \sigma_x & \tau_{xy} \\ \tau_{yx} & \sigma_y \end{bmatrix} \longleftrightarrow \sigma = \begin{bmatrix} \sigma_1 & 0 \\ 0 & \sigma_2 \end{bmatrix} \longleftrightarrow \sigma = \begin{bmatrix} \sigma_1 + \sigma_2 & 0 \\ 0 & \sigma_1 - \sigma_2 \end{bmatrix} \quad (4)$$

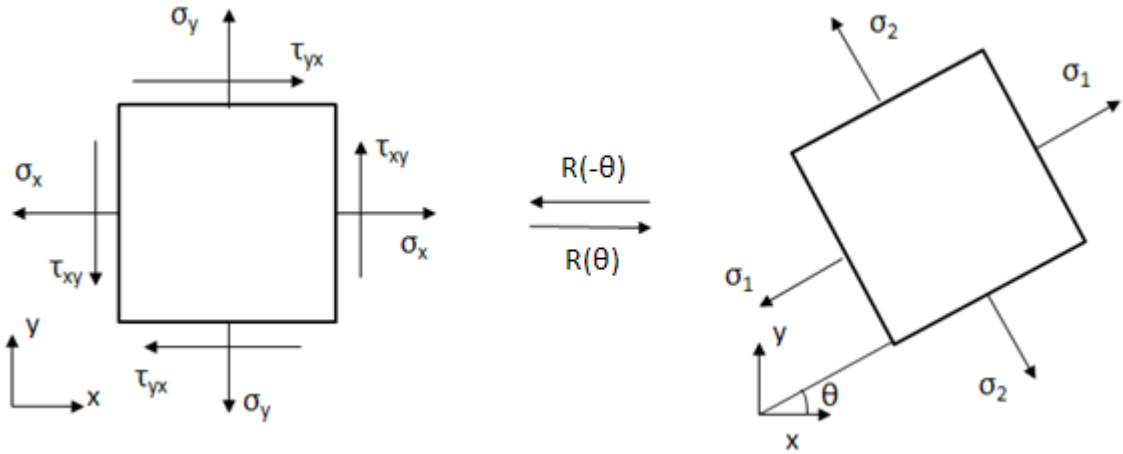


Figure 13: Observation axis rotation of plane stress

2.3 Stress Optical Relationship

The photoelastic effect in some transparent materials has essentially the same optical property as phase retarders/wave plates. The change in polarized refractive index is directly related to the principal stresses experienced at each point in the transparent material. In the case of flat photoelastic material of uniform thickness, the stress to refractive index relationship is described by the Maxwell Neumann Principle. The principle states that the optical axes orientations (i.e., the orientations of the slow and fast polarization axes) are oriented in the same angles as the principal stresses. [18]

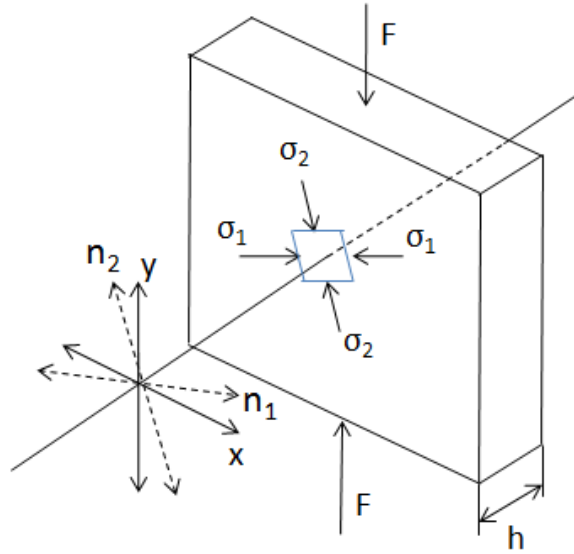


Figure 14: Stress Optical Relationship

Each point in the plane (x,y) in figure 14 experiences a different state of stress relative to its neighbouring point. Due to the plane stress nature of the deformation, the stress does not vary through the depth of the material. The change in refractive indexes due to stress is described in equation set 5, where n is the refractive index of air, n_1 and n_2 are the birefringent refractive indices of the stressed material, and n_0 is the refractive index of the unstressed material before becoming birefringent. The polarization directions of n_1 and n_2 are the same as that of the principal stresses, associated with that particular point. The stress optical coefficients A' and B' are properties of the material.

$$\begin{aligned} n_1 - n &= A'\sigma_1 + B'\sigma_2 \\ n_2 - n &= B'\sigma_1 + A'\sigma_2 \end{aligned} \quad (5)$$

The Maxwell-Neumann Principle however does not take into consideration the dimension changes caused by the deformation. As illustrated in figure 15, the plane stress deformations cause thickness changes from Poisson's effect.

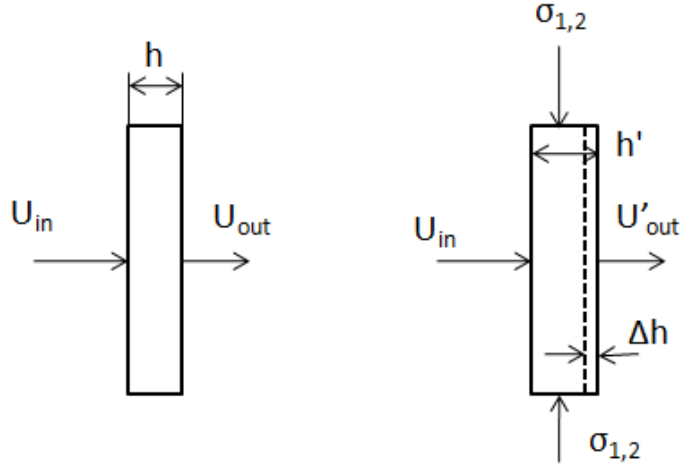


Figure 15: Plane Stress Poisson's Effect

As a light beam enters an unstressed photoelastic specimen (assuming material is residual stress free, and only becomes birefringent when stressed) in figure 15 left, the polarized directional phase change between the light beam entering U_{in} and the exiting U_{out} can be expressed below in equation 6. Φ_1 and Φ_2 are the absolute change in optical phase in the polarization directions of the principal stresses.

$$\Phi_1 = \Phi_2 = \frac{2\pi}{\lambda} hn \quad (6)$$

As stress is applied to the specimen, deformation changes the specimen thickness in figure 15 right (Δh). Most photoelastic materials exhibit isotropic linear elastic behaviour and the change in thickness can be modelled using Hooke's Law below in equation set 7. [12] [18]

$$\Delta h = \frac{h\nu}{E}(\sigma_1 + \sigma_2) \quad (7)$$

$$h' = h + \frac{h\nu}{E}(\sigma_1 + \sigma_2)$$

After deformation (figure 15 right), the phase change between U_{in} and U_{out} is expressed in equation set 8, where Φ'_1 and Φ'_2 are phase changes of light travelling in a stressed material.

The new thickness (h' term) takes in consideration of the change in refractive index from Maxwell Neumann Principle and also the Poisson's effect. While the h term accounts for the beam that used to travel in air before loading.

$$\begin{aligned}\phi'_1 &= \frac{2\pi}{\lambda} (n_1 h' - n_0 h) \\ \phi'_2 &= \frac{2\pi}{\lambda} (n_2 h' - n_0 h)\end{aligned}\tag{8}$$

Substituting equation sets 5 and 7 into equation set 8, the phase change can be rearranged into the following:

$$\begin{aligned}\phi'_1 &= \frac{2\pi}{\lambda} h \left[\left(A' - \frac{n_0 \nu}{E} + \frac{n\nu}{E} \right) \sigma_1 + \left(B' - \frac{n_0 \nu}{E} + \frac{n\nu}{E} \right) \sigma_2 + n + \frac{\nu}{E} A \sigma_1 (\sigma_1 + \sigma_2) \right. \\ &\quad \left. + \frac{\nu}{E} B \sigma_2 (\sigma_1 + \sigma_2) \right] \\ \phi'_2 &= \frac{2\pi}{\lambda} h \left[\left(B' - \frac{n_0 \nu}{E} + \frac{n\nu}{E} \right) \sigma_1 + \left(A' - \frac{n_0 \nu}{E} + \frac{n\nu}{E} \right) \sigma_2 + n + \frac{\nu}{E} A \sigma_2 (\sigma_1 + \sigma_2) \right. \\ &\quad \left. + \frac{\nu}{E} B \sigma_1 (\sigma_1 + \sigma_2) \right]\end{aligned}\tag{9}$$

The terms in equation set 9 that are nonlinear functions of the principal stresses σ_1 and σ_2 can be neglected due to their small size compared with the other terms. [17]

$$\begin{aligned}\frac{\nu}{E} A \sigma_1 (\sigma_1 + \sigma_2) &\approx 0 \\ \frac{\nu}{E} B \sigma_2 (\sigma_1 + \sigma_2) &\approx 0 \\ \frac{\nu}{E} A \sigma_2 (\sigma_1 + \sigma_2) &\approx 0 \\ \frac{\nu}{E} B \sigma_1 (\sigma_1 + \sigma_2) &\approx 0\end{aligned}\tag{10}$$

The relationship between the phase changes from entering to exiting the stressed photoelastic material can be expressed in equations 11. This relationship maintains the linear relation between the principal stress values and the constant coefficients in the Maxwell Neumann stress optical relationship in equation set 5.

$$\begin{aligned}\phi'_1 &= \frac{2\pi}{\lambda} h \left[\left(A' - \frac{n_0\nu}{E} + \frac{n\nu}{E} \right) \sigma_1 + \left(B' - \frac{n_0\nu}{E} + \frac{n\nu}{E} \right) \sigma_2 + n \right] \\ \phi'_2 &= \frac{2\pi}{\lambda} h \left[\left(B' - \frac{n_0\nu}{E} + \frac{n\nu}{E} \right) \sigma_1 + \left(A' - \frac{n_0\nu}{E} + \frac{n\nu}{E} \right) \sigma_2 + n \right]\end{aligned}\quad (11)$$

During the phase stepping process, the unstressed material optical path length is subtracted from that of the stressed material. Thus the final measured phase change from unstressed to stressed material can be expressed in equation set 12, where equation set 11 is combined with equation set 8. A and B are direct stress optical coefficients that taken into account of the thickness variations of the material.

$$\begin{aligned}\varphi_1 &= \phi'_1 - \phi_1 = \frac{2\pi}{\lambda} h [A\sigma_1 + B\sigma_2] \\ \varphi_2 &= \phi'_2 - \phi_2 = \frac{2\pi}{\lambda} h [B\sigma_1 + A\sigma_2]\end{aligned}\quad (12)$$

The principal stresses can be solved from the measured phase change by inverting equation set 12.

$$\begin{aligned}\sigma_1 &= \frac{\lambda}{2\pi h} \left(\frac{A}{A^2 - B^2} \varphi_1 - \frac{B}{A^2 - B^2} \varphi_2 \right) \\ \sigma_2 &= \frac{\lambda}{2\pi h} \left(\frac{-B}{A^2 - B^2} \varphi_1 + \frac{A}{A^2 - B^2} \varphi_2 \right)\end{aligned}\quad (13)$$

2.4 Tensor Field Character of Birefringence

The tensor character of birefringence phase change in photoelastic materials is illustrated for the case where the principal axis orientation is known in figure 11. The optical phase shift along the principal stress directions (x, y) follows the stress optical relationship in equations 12. The Jones matrix to express this change is:

$$\begin{bmatrix} U_x \\ U_y \end{bmatrix}_{\text{out}} = \begin{bmatrix} u & 0 \\ 0 & v \end{bmatrix} \begin{bmatrix} U_x \\ U_y \end{bmatrix}_{\text{in}} \quad (14)$$

where u and v are the principal complex transmission factors that take into account attenuation and phase change due to birefringence. Since stress-optical effects only influence refractive index, there is no attenuation effect, and thus the complex transmission factors have unit magnitudes.

$$\begin{aligned} u &= e^{i\varphi_1} \\ v &= e^{i\varphi_2} \end{aligned} \quad (15)$$

In the general case where the principal axis orientation is unknown, the principal axis inclines at an angle θ with the observation axis. The Jones matrix undergoes a geometric axis transformation:

$$\begin{bmatrix} U_x \\ U_y \end{bmatrix}_{\text{out}} = \begin{bmatrix} \cos\theta & -\sin\theta \\ \sin\theta & \cos\theta \end{bmatrix} \begin{bmatrix} u & 0 \\ 0 & v \end{bmatrix} \begin{bmatrix} \cos\theta & \sin\theta \\ -\sin\theta & \cos\theta \end{bmatrix} \begin{bmatrix} U_x \\ U_y \end{bmatrix}_{\text{in}} \quad (16)$$

Equation 16 can be expanded into equation 17, which contains the familiar relationship for axis transformation of second-order tensor quantities [14]. For typical second-order tensor quantities such as stress, strain and moments/products of inertia, the terms in equation 17 are all real, but in the present case of phase change during light transmission, the terms are

complex numbers Off-diagonal terms in the Jones matrix correspond to light in orthogonal polarization.

$$\begin{bmatrix} U_x \\ U_y \end{bmatrix}_{\text{out}} = \begin{bmatrix} \frac{u+v}{2} + \frac{u-v}{2} \cos 2\theta & \frac{u-v}{2} \sin 2\theta \\ \frac{u-v}{2} \sin 2\theta & \frac{u+v}{2} - \frac{u-v}{2} \cos 2\theta \end{bmatrix} \begin{bmatrix} U_x \\ U_y \end{bmatrix}_{\text{in}} \quad (17)$$

Placement of polarization filters in front and behind the specimen can isolate each element in the Jones matrix. Through the use of the Mohr's circle relationship, the principal complex transmission factors u and v can then be calculated. For example by setting both polarization filters to the horizontal, the depolarization components and the vertical polarization components can be filtered and isolates only the top left element. The depolarized elements can be isolated by orienting the polarization filters orthogonal to each other. Such method is impractical due to the absence of light passing through the polarization filters. To solve this issue, four sets of phase measurements are taken with both polarization filters in front and behind the specimen oriented parallel and each measurement taken at 45° apart as illustrated below in figure 16.

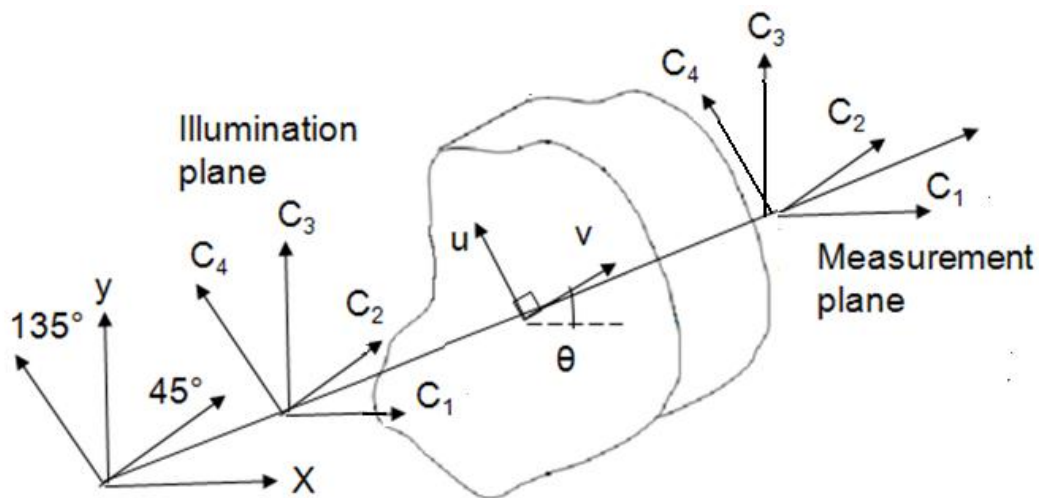


Figure 16: Polarization Measurement of Photoelastic Material

Quantities p represents the isotropic component of the complex transmission factors, while q and t represent the deviatoric components. Analogous quantities are used in planar stress analysis, where p is the hydrostatic stress, t is the axial shear stress, and q is the shear stress at 45° to the axis. [19] Equation 18 can be tabulated into matrix representation and rearranged into the following:

$$\begin{bmatrix} 1 & 1 & 1 & 1 \\ 1 & 0 & -1 & 0 \\ 0 & -1 & 0 & 1 \end{bmatrix} \begin{bmatrix} C_1 \\ C_2 \\ C_3 \\ C_4 \end{bmatrix} = \left\{ \frac{u}{2} \begin{bmatrix} 4 & 0 & 0 \\ 0 & 2 & 0 \\ 0 & 0 & 2 \end{bmatrix} + \frac{v}{2} \begin{bmatrix} 4 & 0 & 0 \\ 0 & -2 & 0 \\ 0 & 0 & -2 \end{bmatrix} \right\} \begin{bmatrix} 1 \\ \cos 2\theta \\ \sin 2\theta \end{bmatrix} \quad (19)$$

Coincidentally the left side of matrix equation 19 is similar to the features on Mohr's circle in figure 17. The relationship between the isotropic and deviatoric components of the transmission factors (p , q , and t) and the measured transmission factors is represented below in equation set 20.

$$\begin{aligned} p &= \frac{u+v}{2} = \frac{(C_1 + C_2 + C_3 + C_4)}{4} \\ q &= \frac{u-v}{2} \cos 2\theta = \frac{(C_1 - C_3)}{2} \\ t &= \frac{u-v}{2} \sin 2\theta = \frac{(C_4 - C_2)}{2} \end{aligned} \quad (20)$$

The principal complex transmission factors (u and v) and principal axis orientation (θ) can be solved in the same manner as principal stresses from normal and shear stress quantities.

$$\begin{aligned} u, v &= e^{i\varphi_1}, e^{i\varphi_2} = p \pm \sqrt{q^2 + t^2} \\ \theta &= \frac{1}{2} \tan^{-1} \frac{t}{q} \end{aligned} \quad (21)$$

2.5 Phase Stepping Interferometry

Interferometry allows precise measurements of the phase of light beams [20]. Figure 18 shows the interaction of two monochromatic light beams of the same wavelength, amplitudes and polarization. Constructive interference occurs where the waves are in phase and destructive interference occurs when the waves are 180° out of phase. As the relative phase changes between the two waves, the optical intensity of the interference changes from bright in the constructive interference case to dark in the destructive interference case.

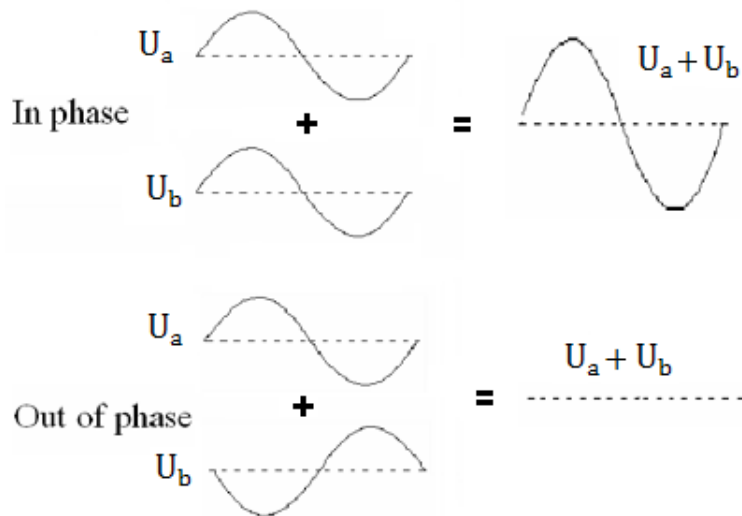


Figure 18: Superposition of Electromagnetic Fields

The complex amplitude at any point in the interference pattern is the sum of the complex amplitudes of these two waves. Assuming one of the beams passes through an unstressed photoelastic specimen, while the other passes through empty space. These two waves can be mathematically expressed as:

$$\begin{aligned}
 U_a &= |U_a|e^{i\phi_a} \\
 U_b &= |U_b|e^{i(\phi_b + \beta_n)}
 \end{aligned}
 \tag{22}$$

The optical intensity of a wave is the square of its electromagnetic wave amplitude. The intensity of the super-positioned wave is thus a function of the amplitudes $|U_a|$ and $|U_b|$ of the two separate waves and their phase difference $\Phi_a - \Phi_b$. Phase stepping algorithm is used to determine the phase different between the two beams ($\Phi_a - \Phi_b$). Since optical sensors can only detect intensity and not phase, the intensity of the super-positioned wave (I) has to be altered by the constant β_n to create a set of unique intensity values (I_1, I_2, I_3, I_4) illustrated in figure 19. The value of β_n exists as integer multiples of $\pi/2$.

$$I = |U|^2 \quad (23)$$

$$I = |U_a + U_b|^2$$

$$I = \underbrace{|U_a|^2 + |U_b|^2}_G + 2 \underbrace{\sqrt{|U_a|^2 |U_b|^2}}_H \cos(\Phi_a - \Phi_b + \beta_n)$$

When stress is applied to the specimen, the phase of the beam passing through changes from Φ_a to Φ'_a . The constant amplitudes of the two beams means that the intensity I is a function of the phase difference ($\Phi'_a - \Phi_b$) and the known phase step value β_n . G is the average intensity of the phase stepped intensity image and G is the modulation of light from the phase stepping.

$$U'_a = |U_a| e^{i\Phi'_a} \quad (24)$$

$$U_b = |U_b| e^{i\Phi_b + \beta_n}$$

$$I = G + H \cos(\Phi'_a - \Phi_b + \beta_n) \quad (25)$$

Figure 19 graphically illustrates the phase stepping algorithm. Sets of phase-stepped images are taken before and after applying stress to the photoelastic material. After applying stress, the intensity I follows a different pattern due to the change in phase from Φ_a to Φ'_a , while the phase of the reference beam remains constant.

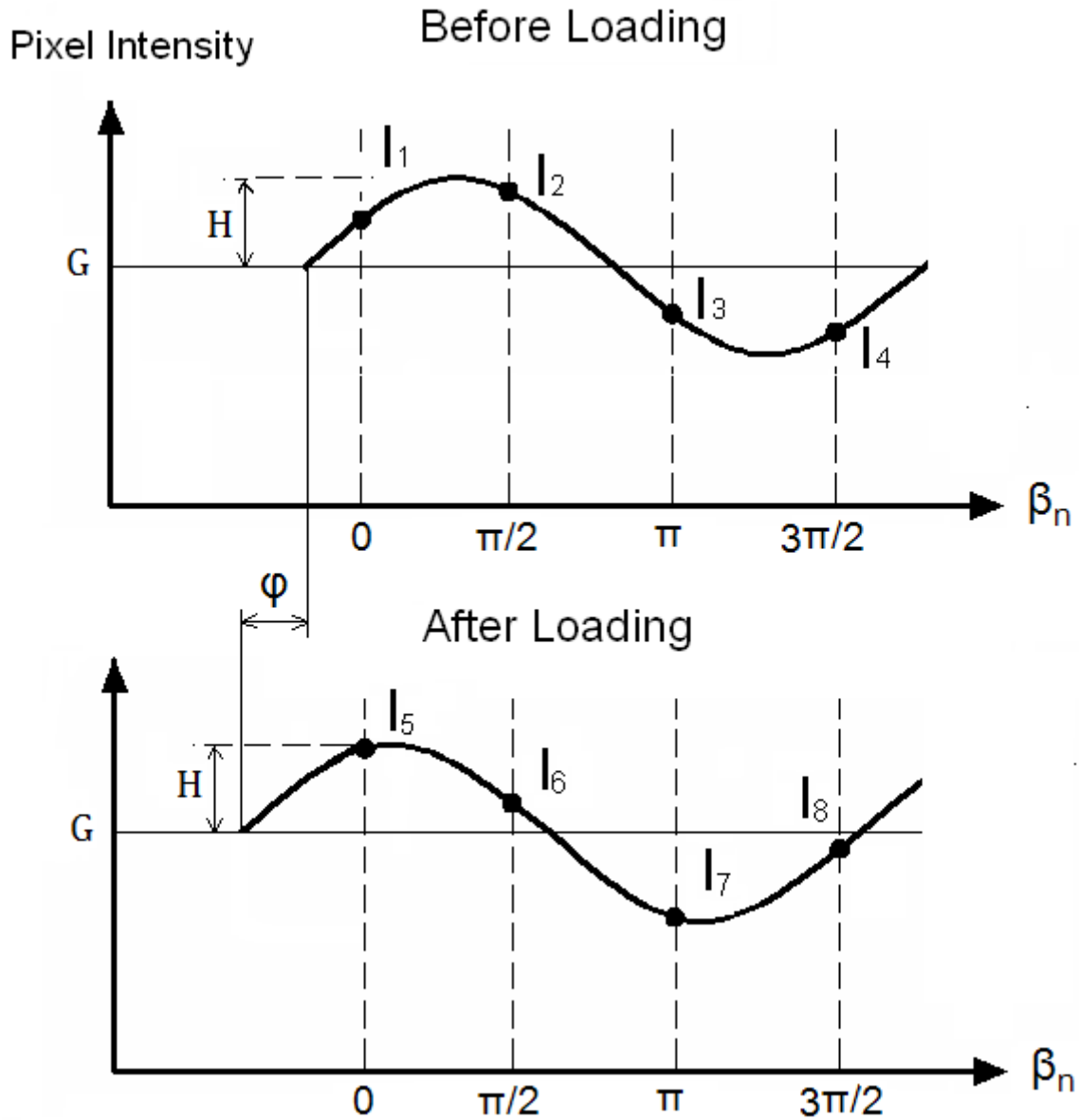


Figure 19: Phase Stepping Algorithm

The phase differences calculations between the two beams are expressed in equations sets 25 and 26. [21] The change in phase difference between the two beams is subtracted from each other to create a phase map φ in equation 27. This value is the same as the one expressed in equation 12. With the placement of polarization filters, the measured change in phase

difference is that of the polarized component of the beam passing through the photoelastic material.

$$\tan (\phi_a - \phi_b) = \frac{I_2 - I_4}{I_1 - I_3} \quad (25)$$

$$\tan (\phi'_a - \phi_b) = \frac{I_6 - I_8}{I_5 - I_7} \quad (26)$$

$$\varphi = (\phi'_a - \phi_b) - (\phi_a - \phi_b) \quad (27)$$

Substituting the phase angles from equation 27 into equations 20 and 21 gives the principal attenuations u and v and the principal direction θ . This calculation is applied to every pixel within the measured optical images and thus a full-field stress evaluation is achieved.

2.6 Far Field Drift Compensation

One of the challenges in optical phase measurements is that the refractive index of air is dependent on air pressure, and any differential change in air pressure causes disturbances in the phase measurements [22]. Even though preventative measure such as an enclosed cabinet is used to isolate the optical equipments, compensation technique is still necessary to correct this. The change in pressure is time dependent. As time passes by between the two sets of phase shifting measurements, the disturbance accumulates to a drift in the measurements as mathematically expressed below in the phase shifting equation similar to equation 28, where β_n is the drift in phase due to change in air pressure. During the phase shifting evaluation of the phase change

$$I = G + H \cos (\phi'_a - \phi_b + \beta_n + \alpha) \quad (28)$$

over time, both the photoelastic and drift phase changes are evaluated together, resulting in an inaccurate measurement. A useful characteristic of this disturbance is that the effect across the measurement image has very low gradient, i.e. effect on each camera pixel is equal to another. The solution to this is to evaluate the phase changes in the far field of the sensor image as illustrated below in figure 20.

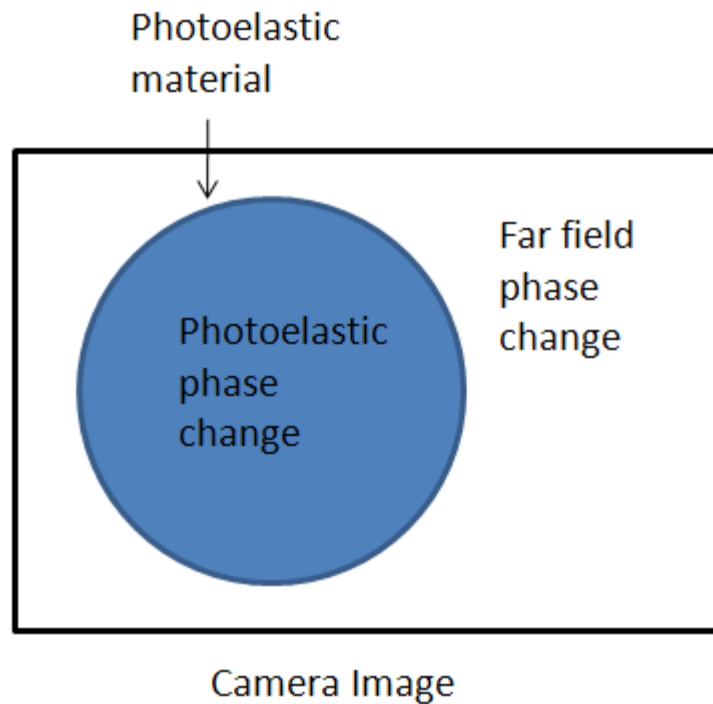


Figure 20: Drift Compensation by Far Field Phase Subtraction

Since the far field phase change is independent of photoelastic phase change, the phase change over time in those image pixels should be zero as expressed below. This allows the phase drift value α to be evaluated. With the value of α known, the phase values of the pixels in the photoelastic material can be subtracted by α to determine the correct photoelastic phase change.

$$\phi'_a - \phi_b = 0 \quad (29)$$

Chapter 3 – Modifications to Interferometric Photoelastic Measurement Method

3.1 Introduction to Interferometric Photoelasticity

The simplicity of classical photoelasticity makes it an attractive experimental technique; only a pair of polarizing filters is required to observe stress induced fringes in a photoelastic test material. Observation of isoclinic fringes is also straightforward, although rather tedious. In comparison, interferometric photoelasticity requires a much more complex and environmentally sensitive optical arrangement consisting of an interferometer with precision mechanical alignments [23]. However, once the equipment is set up, the required measurements are simple and compact.

The main advantage of using interferometric photoelasticity is that the third stress component of principal stress sums are present in the measurement, where they are absent in the classical method. Another advantage is that the polariscope arrangement can be integrated in a Mach-Zehnder interferometer allowing both measurements are possible with one experiment setup, as illustrated in figure 6 [11]. In comparison with other methods such as combining classical photoelastic measurements with that of thermoelasticity, two separate experiment arrangements are needed, in order to obtain full-field stress distributions of all three components of in-plane stresses [13].

The proposed measurement method can be considered as an extension of interferometric photoelasticity. Treating photoelastic birefringence as a tensor quantity simplifies the number of measurements needed to extract all three components of in-plane stresses to at least three sets of phase stepped measurements. Limitations and challenges to

current interferometric measurement methods such as measurement sensitivity, size of field of view, and alignment procedures are also addressed in the proposed experiment configuration.

3.2 Proposed Experiment Configuration

To characterize the tensor quality of photoelastic birefringence, the optical path length changes for a stressed photoelastic material needs to be identified. To accomplish this, a Michelson type interferometer is proposed for this application, as illustrated in figures 21 and 20. The optical arrangement features a two-stage beam expansion to image specimens of dimensions that are larger than that of the beamsplitter. A piezo-electric actuator attached to one of the mirrors actuates the phase shifting measurements. The placement of the polarization filter on the specimen arm of the interferometer allows specific polarization components of the phase changes to be evaluated. The phase changes correspond with that of the directional transmission factors illustrated in figure 16.

Although Mach-Zehnder type interferometers have been typically used for this application, and both interferometers can implement phase stepping measurements to determine phase changes in one of their optical path lengths [20][22]. From a conceptual perspective, the Michelson interferometer is a folded variation of the Mach-Zehnder interferometer. For the application of measuring phase shift due to photoelastic birefringence, the Michelson setup effectively doubles the optical thickness of the photoelastic specimen and thus doubles the birefringence effect and the measurement sensitivity. Another advantage of the Michelson arrangement is the reduction of the optical components needed: only one beamsplitter and a pair of beam expansion lenses are required compared to two beamsplitters and two pairs of beam expansion lenses in the Mach-Zehnder.

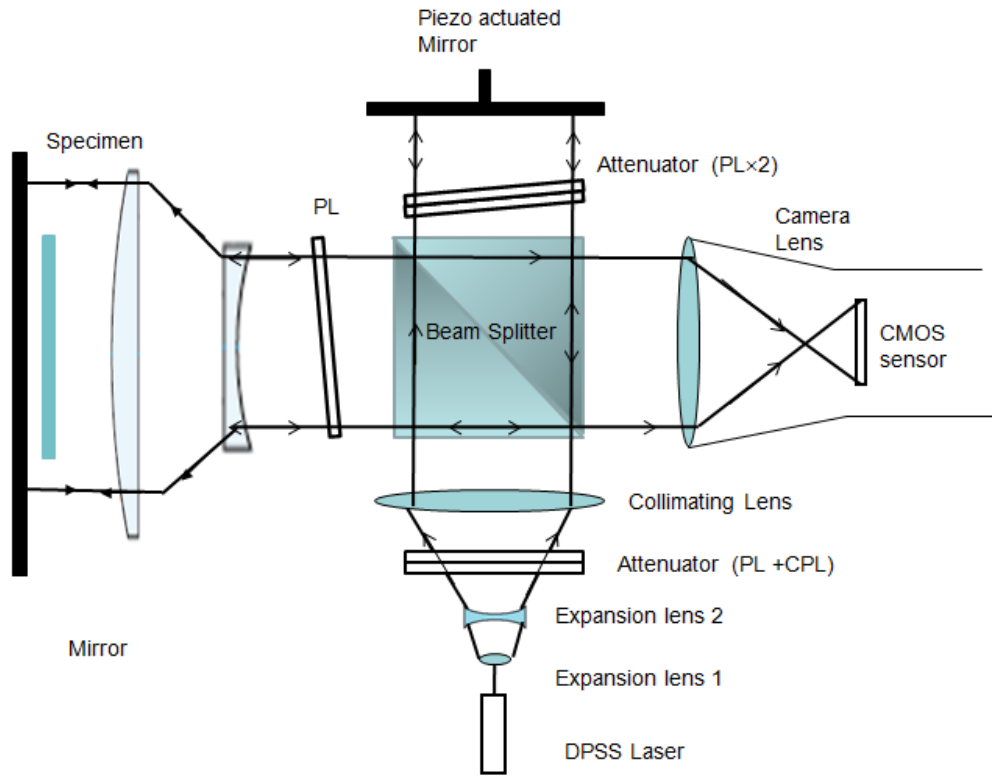


Figure 21: Optical layout of interferometer

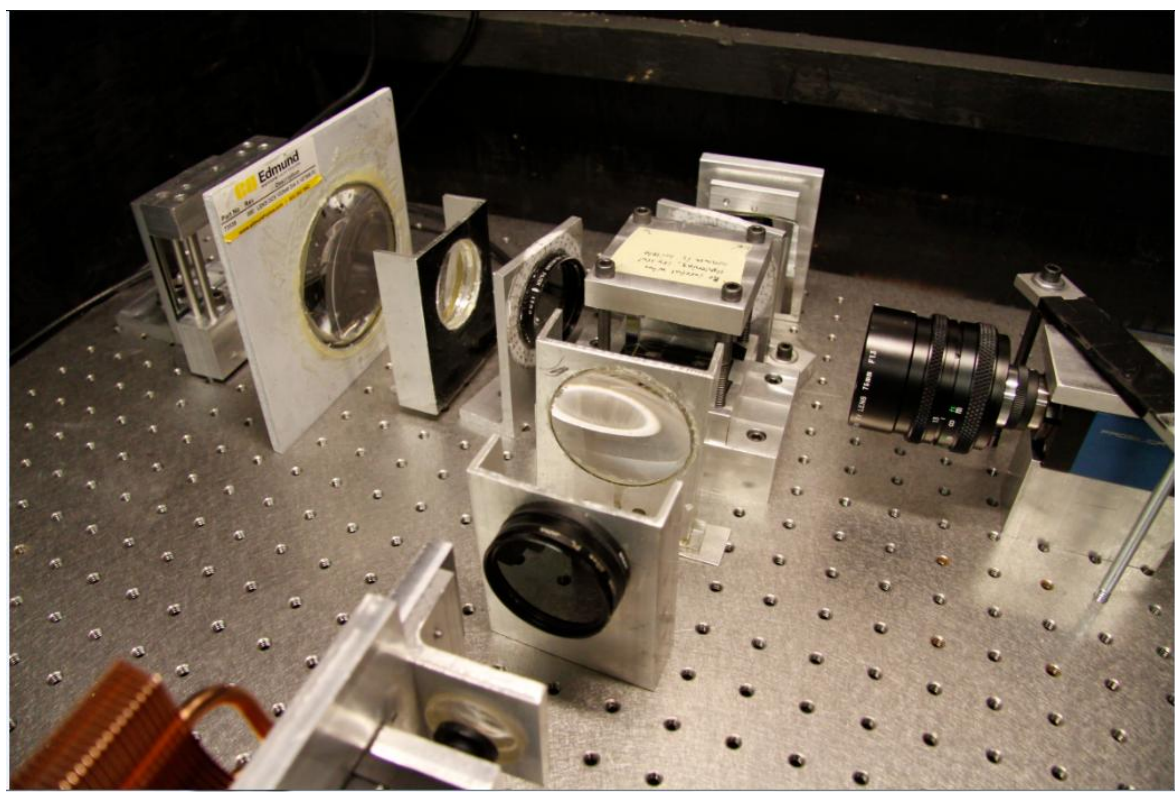


Figure 22: Experiment optical equipment

3.2.1 Secondary Beam Expansion

In typical interferometer arrangements, the field of view is limited by the size of beamsplitters and illumination beam diameter. The second beam expander placed in front of the specimen effectively resolves this problem. It allows specimens of dimensions larger than the beamsplitter to be imaged. The optical arrangement can also function without the second beam expander, allowing more detailed measurements of smaller specimens.

The first stage beam expander expands the laser beam for both interferometer arms. A diode pumped solid state laser (DPSS) is used to provide stable and coherent illumination. The first two lenses in front of the laser expand the millimetre wide beam, while the larger convex lens focuses the diverging beam back into parallel form. Figure 23 shows the optical diagram of the lenses used, the laser beam is expanded 80 times the original diameter.

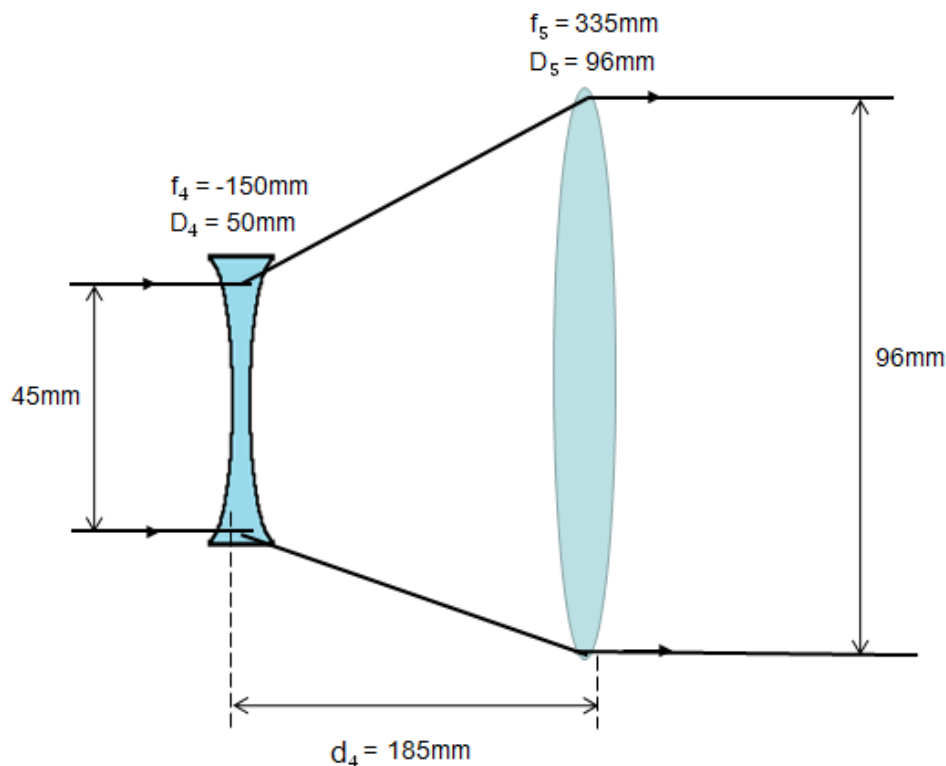


Figure 23: Ray Diagram of Laser Beam Expansion

The second stage beam expander closely resembles the first stage expander; a convex lens diverges the incoming collimated beam from the beamsplitter and the concave lens collimates it, as schematically shown in figure 24. The returning beam reflected back from the mirror follows the same optical path, but in opposite direction

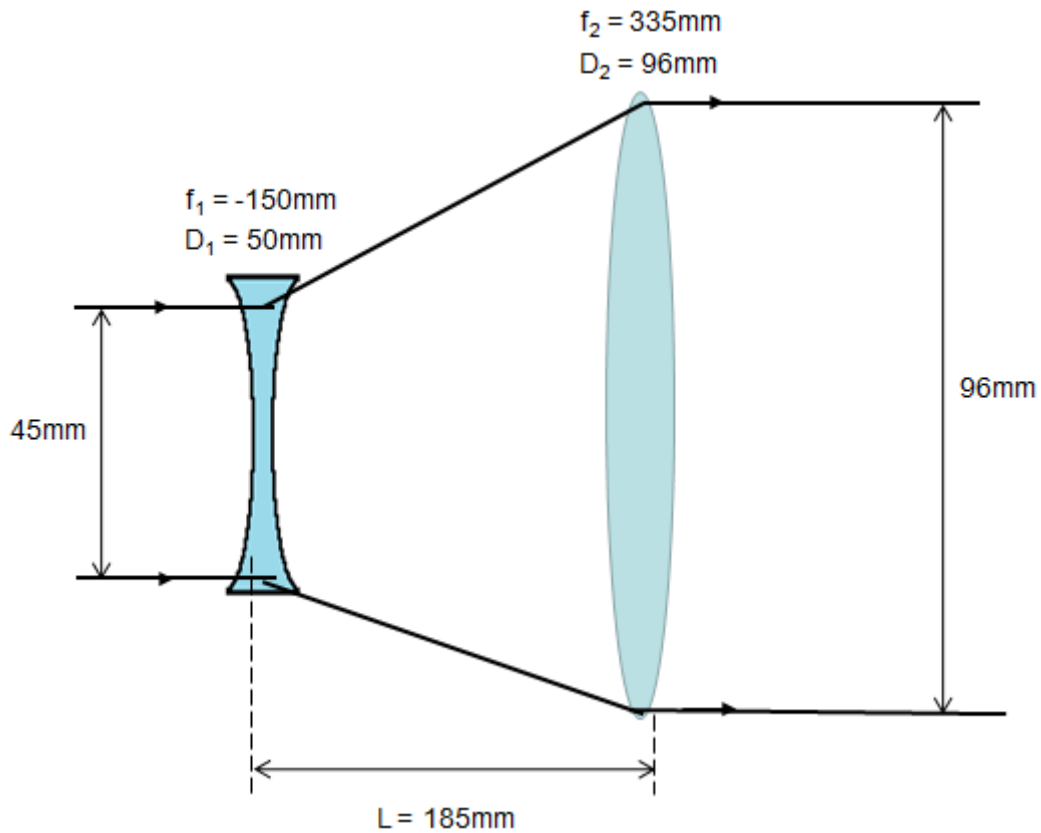


Figure 24: Ray Diagram of Second Stage Beam Expander

The second stage beam expander has a magnification power of 2.2 times. Its main purpose is to demonstrate that the field of view of this optical arrangement is not limited by the size of beamsplitter and camera lens. Cube beamsplitters are relatively expensive and difficult to manufacture in large sizes compared to plate beamsplitters, but they do not suffer from the internal reflection problems of plate beamsplitters. [23]

The main challenge of light beam passing twice through the specimen in the Michelson configuration is that the beam may not be accurately parallel. This causes a double image to appear on the camera sensor, as shown in figure 25. The misalignment can be corrected by adjusting the horizontal position offset between the center of the expanded laser beam and the position of the collimating lens.

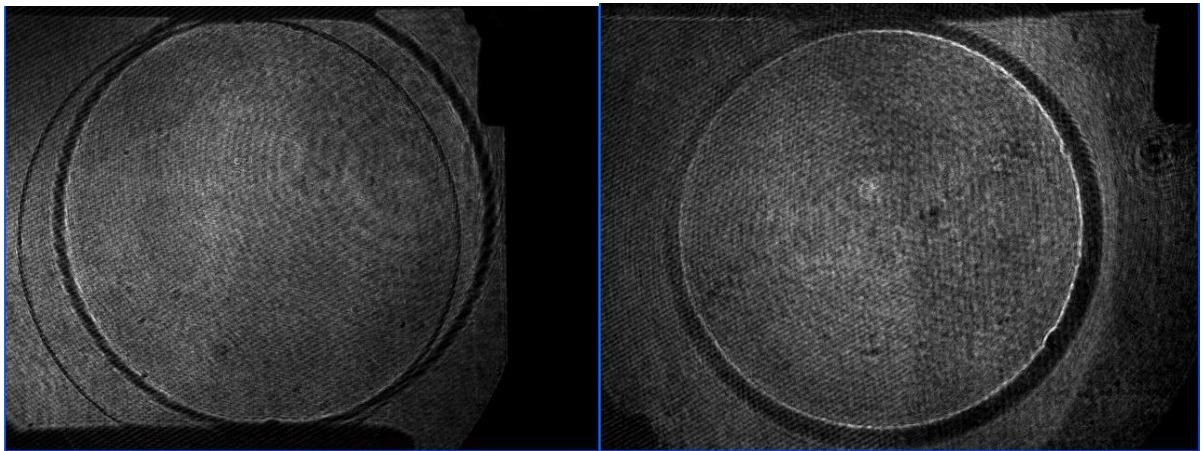


Figure 25: Double Image Due to Collimation Lens Misalignment

3.2 .2 Optical Phase Detection

A C-mount imaging lens attached to a digital CMOS sensor is used to measure the intensity change resulting from the phase change between the two arms of the interferometer. Because of the parallel beam arrangement within the interferometer, the beam within the camera passes through a focal point ahead of the sensor plane, as shown in Figure 26. The distance d needed to project the collimated beam to the size of the CMOS sensor can be experimentally determined by placing extension tubes between the lens and camera lens mount. For the measurements reported here, a 10mm long extension washer gave appropriate magnification with focal length $f=12.5\text{mm}$ lens and lens diameter of 75mm.

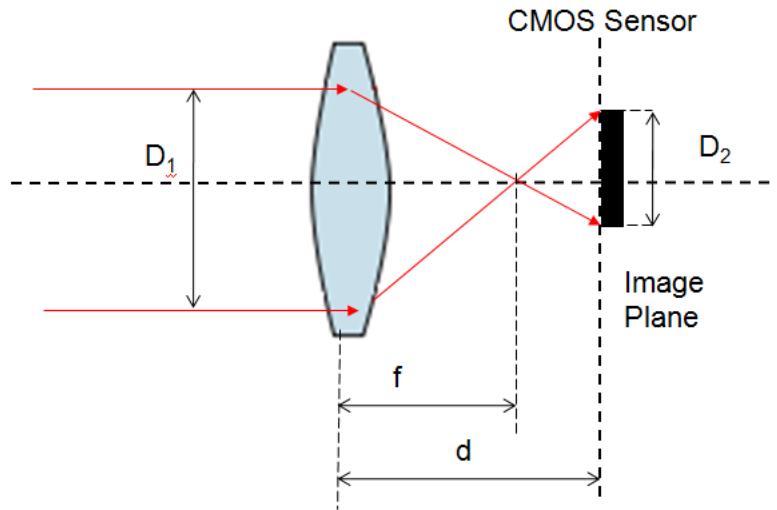


Figure 26: Ray Diagram of Camera Lens

3.2.3 Phase Shifting Implementation

Phase shifting is used to quantify the change in optical path length between the two arms of the interferometer: A piezo-electric (PZT) stack is used to actuate one of the two mirrors in the phase stepping measurement process described in section 2.5. The piezo stack is attached between the screw adjusted mount and the glass mirror as shown in figure 27. The mirror moves in the direction of the PZT stack, shortening or lengthening the optical path difference between the two beams of the interferometer in quarter of wavelength intervals. The stepping actuation is synchronized with the camera to produce a set of 4 phase stepped images. The incremental stepping process avoids the hysteresis characteristic of the actuator.

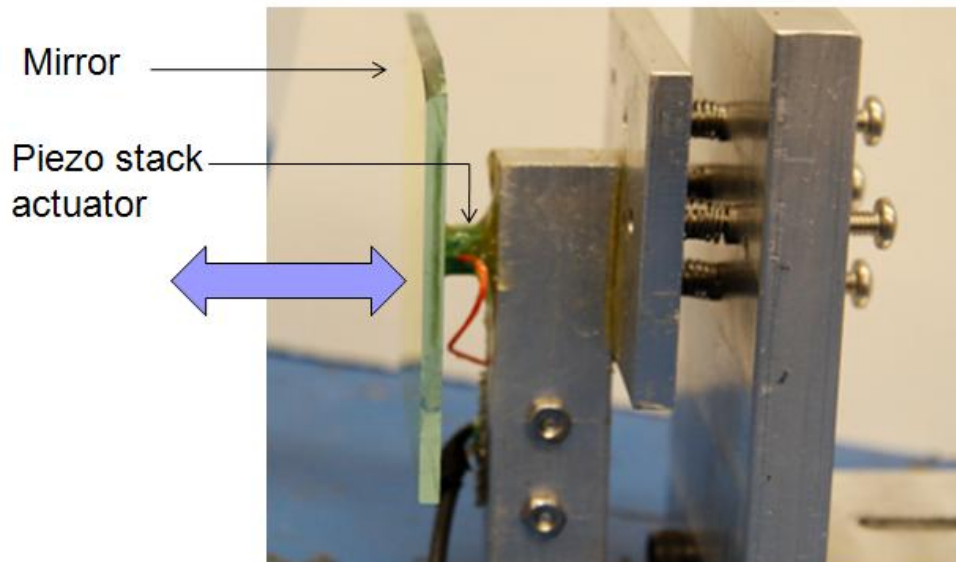


Figure 27: Piezo-Electric Actuated Mirror

Figure 28 shows a set of four phase stepped images taken with the piezo-actuated mirror positioned at quarter wavelength apart. The disk in the center of the image is a circular disk shaped photoelastic specimen. These images correspond with the intensity vs. piezo position function described in figure 19.

After stress is induced in the photoelastic specimen, another set of four phase shifted images are taken. By processing the intensity of each camera pixel according to equation 25 in section 2.5, each pixel's phase change can be calculated. The calculated phase map is presented in figure 29. The white regions of the phase map indicate phase change in multiples of 2π radians, while the black regions indicate phase change in the multiples of π radians. This phase map is affected by the air pressure drift as described in section 2.6. To correct this, the far field (parts of the image that does not contain the specimen) is averaged and subtracted from the entire phase map, resulting in a cleaner measurement as shown in 28.

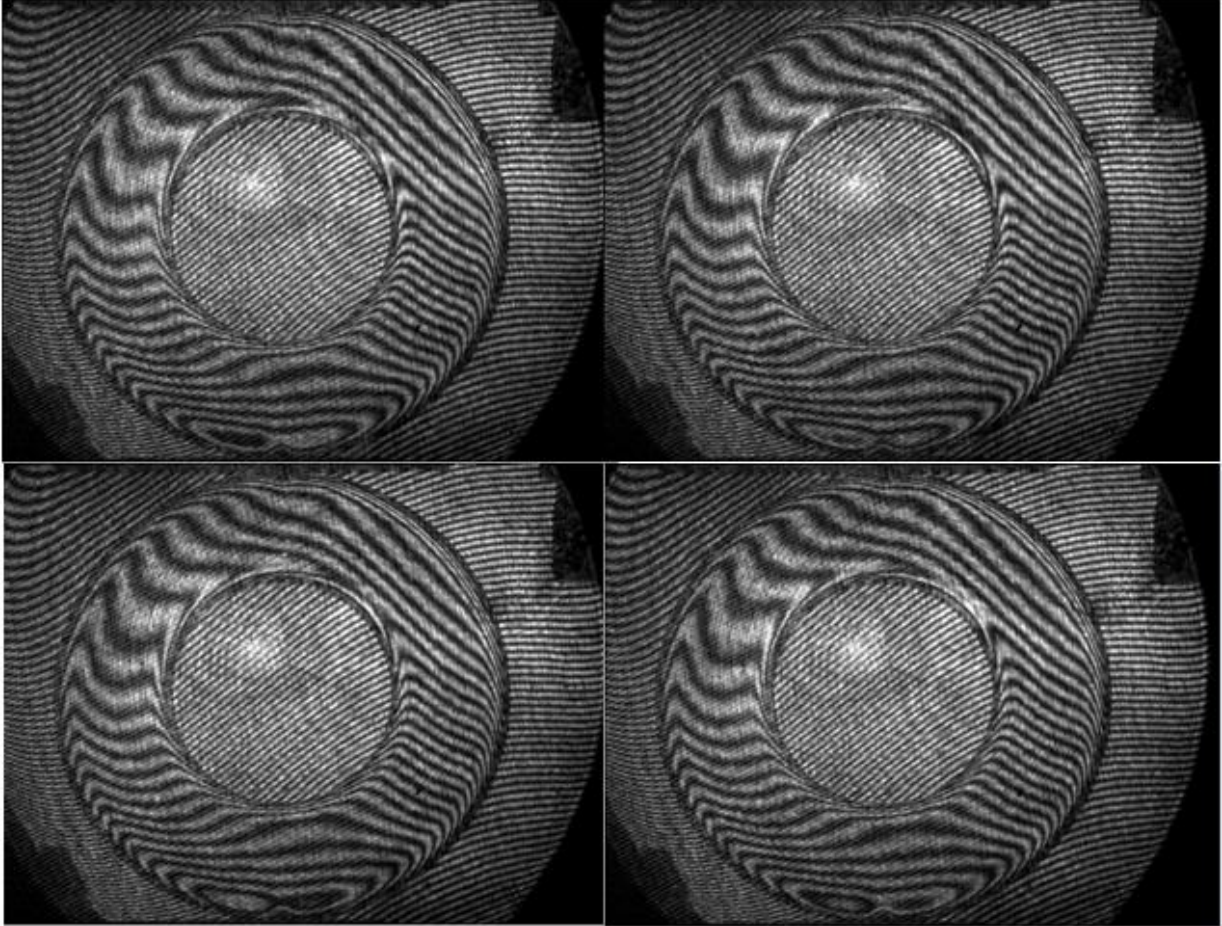


Figure 28: Phase Shifted Measurement Images

Because of the cyclic nature of phase fringes, unwrapping is used to linearize the measurements [24]. The tensor character of birefringence as described in chapter 2 can be mathematically constructed from experimental phase measurements; by taking phase shifting measurements at various polarization angles.

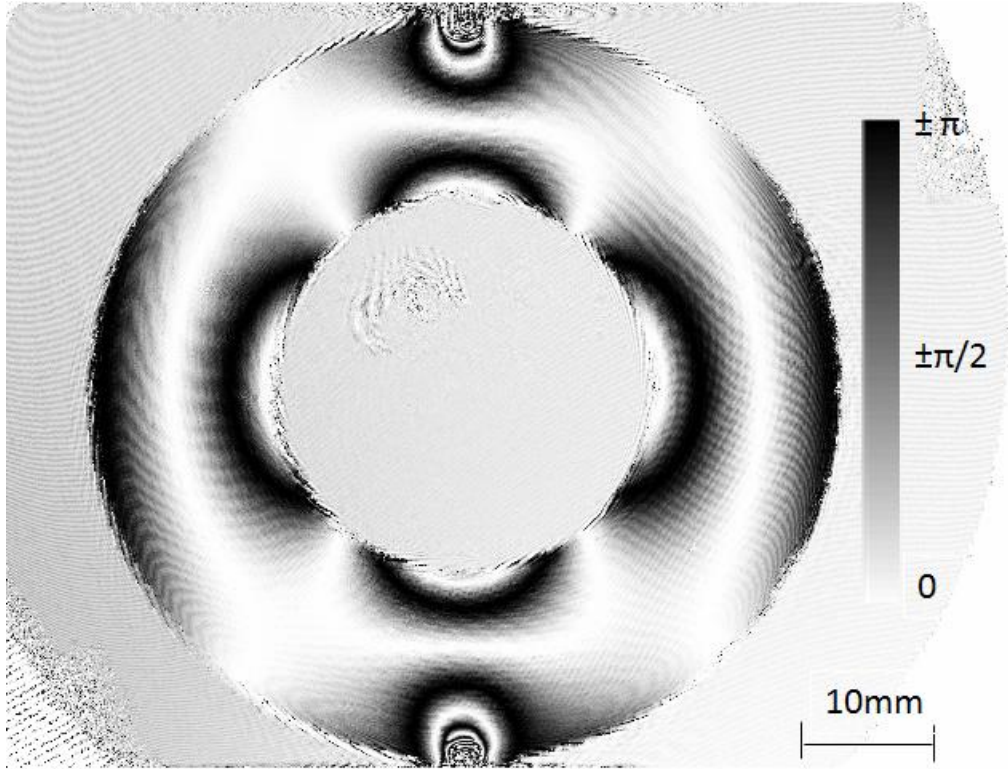


Figure 29: Computed Phase Map

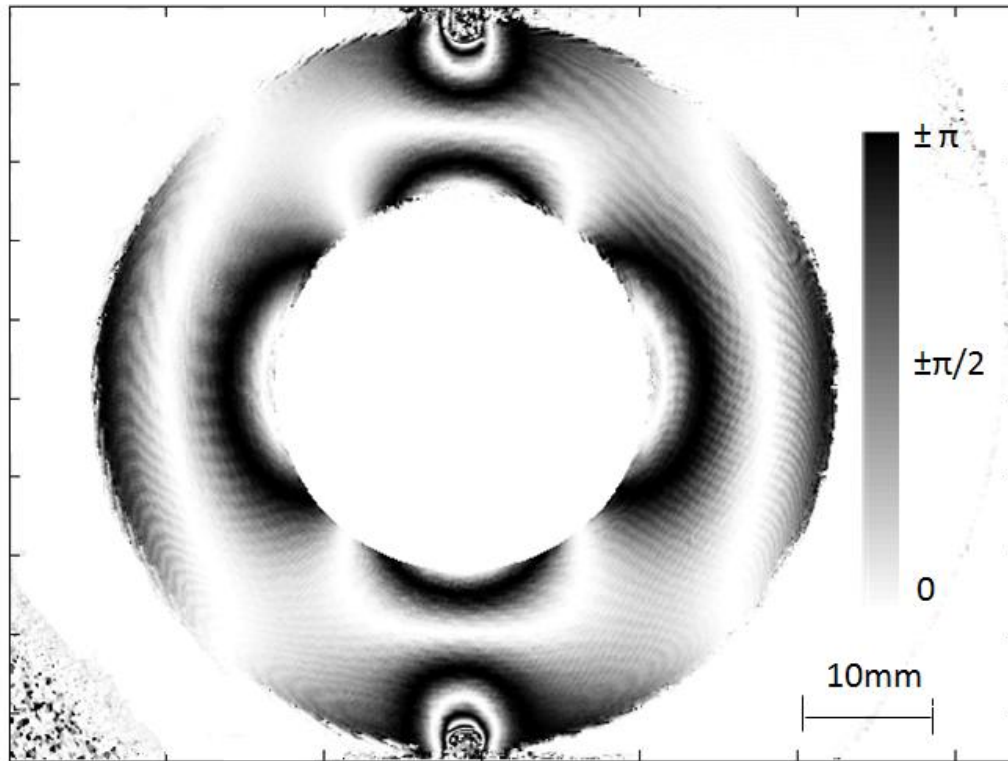


Figure 30: Far Field Drift Subtraction

3.2.4 Polarization Control

Polarizing filters are used to both control the polarization of the beam travelling through the specimen and control the beam intensities of various parts of the arrangement. Plane polarization filters with angular position indication is used to select the desired polarization component to perform phase stepping measurements, as shown below in figure 31.

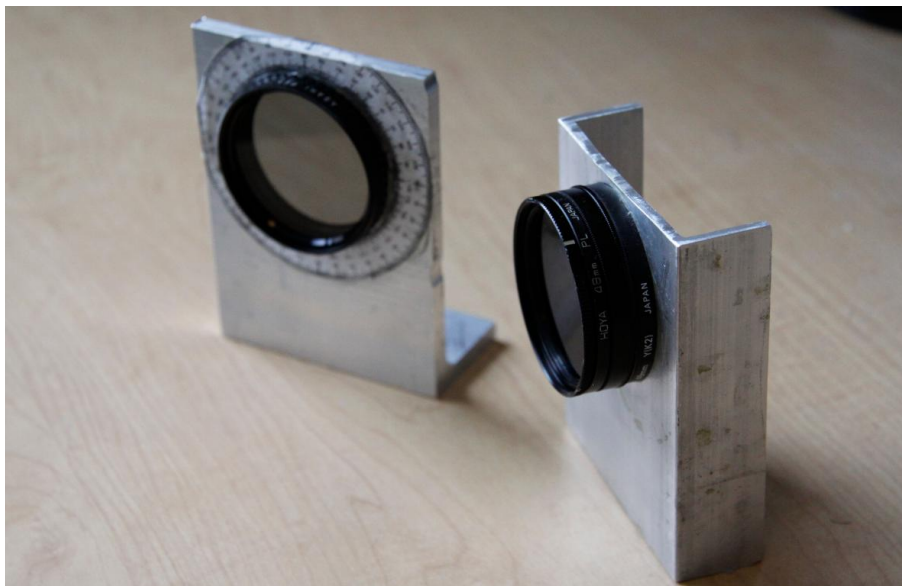


Figure 31: Plane Polarizing Filter and Attenuator

An attenuator is assembled by combining two polarization filters. This arrangement is used to adjust the intensity at the laser output and also to balance the intensity difference between the two interferometer arms. The attenuator on the laser is composed of one plane polarization filter and one circular polarization filter, with its quarter wave plate facing the outside. This configuration essentially unpolarizes the linear polarized output of the laser. The polarization filters are commercial photography filters with a diameter of 49mm.

The alignment of these components is offset by about two degrees to minimize reflection from the surfaces of the filters to the camera. Each filter has a reference mark indicating the direction of polarization. Angular scales are placed around the filters for readout. During testing, both attenuators in front of the laser and on the reference arm can be adjusted to compensate for the change in intensity from the change in polarization on the specimen arm and the uneven polarizing property of the beamsplitter. The polarization angle of the polarizing filter on the specimen arm and that of the polarizing filter on the attenuator closer to the beam splitter must be the same because interference can only take place between beams of the same polarization. [16][26]

3.3 Tuning and Adjustment

In order to achieve nanometre level accurate phase shifted measurements, careful adjustment of the interferometer equipment is necessary [23]. The goal of the adjustment process is to create interference fringes between the two beams of the interferometer.

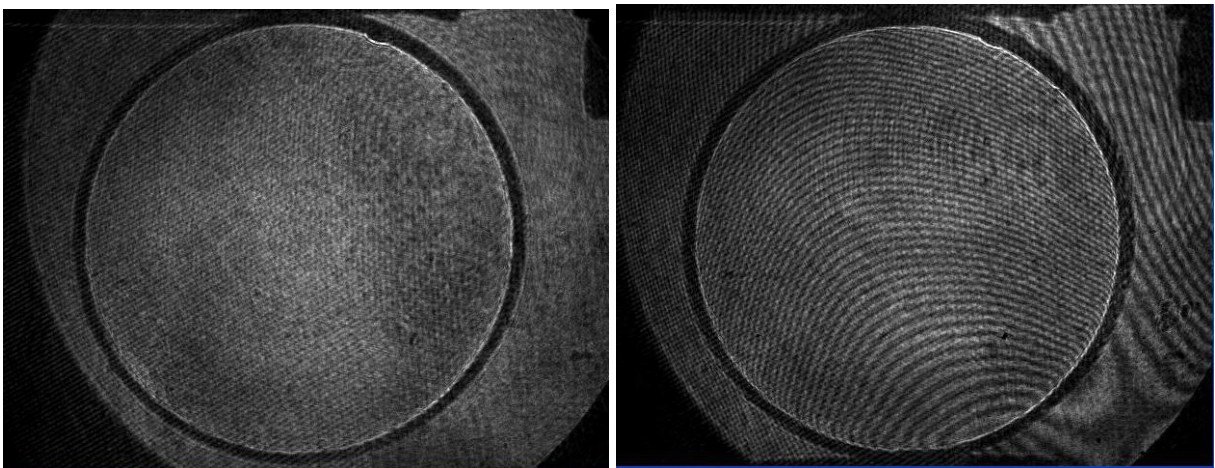


Figure 32: Final Adjusted Two Beam Interference

The following is a list of alignments and adjustments necessary for high quality interference images.

1. Laser expansion alignment is shown in figure 23, the exiting collimated beam should be parallel with an even intensity distribution. The divergence angle of the beam can be adjusted by positioning the position of the collimating lens. The center of illumination can be positioning by moving the first expansion lens.
2. The beamsplitter should be placed squarely as possible, with the center of the cube aligned with the center of the collimated laser beam
3. The imaging camera should be placed at a slight offset angle w.r.t. the beamsplitter to prevent internally reflected beam (of beamsplitter) from entering the camera
4. Beam attenuators and polarization filter should be placed with slight offsets to prevent surface reflections of these optical pieces from entering into the camera lens. The attenuators need to be adjusted before opening the camera aperture, to prevent saturation and damage of the camera sensor.
5. Mirrors on each interferometer arm should be adjusted with positioning screw for correct angular alignment. The centers of each beam can be determined by reducing the camera lens aperture. The correct alignment camera image is shown in figure 32 (left)
6. Second stage beam expander is adjusted in the same manner as the laser beam expander

Figure 32 shows the difference in interference image quality between a well tuned interferometer (right image) and one that is not (left). Interference fringes are clearly visible in the right image. The result is that phase stepping can be detected by the camera.

The formation of the fringes can be explained by modelling two beams as two plane waves intersecting at oblique angles as shown in figure 33. As the two wave intersect at a large angle, a large number of narrow interference fringes form [16][22]. As the oblique angle between the two beams decreases, the interference fringes become further apart. During phase shifting, movements of the interference fringes are visible throughout the image. One noticeable feature of the fringes as shown in figure 32 is that they are very sensitive to the elastic deformation of the setup.

A disadvantage of the Michelson arrangement in comparison with the Mach-Zehnder is the presence of internal reflection in the cube beamsplitter used. This becomes problematic during the alignment process of the two mirrors. The internally reflected beam can form interference patterns with the two main beams of the interferometer. It was found that the additional interference pattern causes excessive measurement noise during phase shifting. The practical solution is to offset the internally reflected beam on the camera sensor by a few degrees. The slight offset creates an angle between the main beams of the interferometer with the internally reflected beam, and causes the noise interference to be less visible to the imaging sensor.

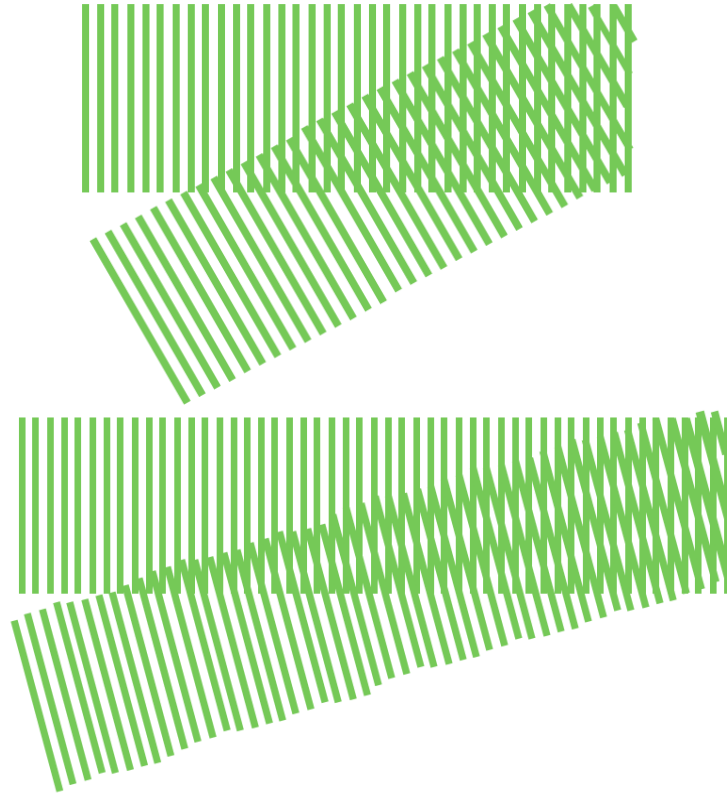


Figure 33: Interference of Two Oblique Plane Waves

The internally reflected beam is caused by the surfaces on the back and left of the cube, where they partially reflect the transmitted beam and reflected beam into the direction of the camera. [23] This is illustrated in figure 34. The Mach-Zehnder arrangement does not suffer from this, because the surface of the beamsplitter with the internal reflection faces away from the rest of the optical components.

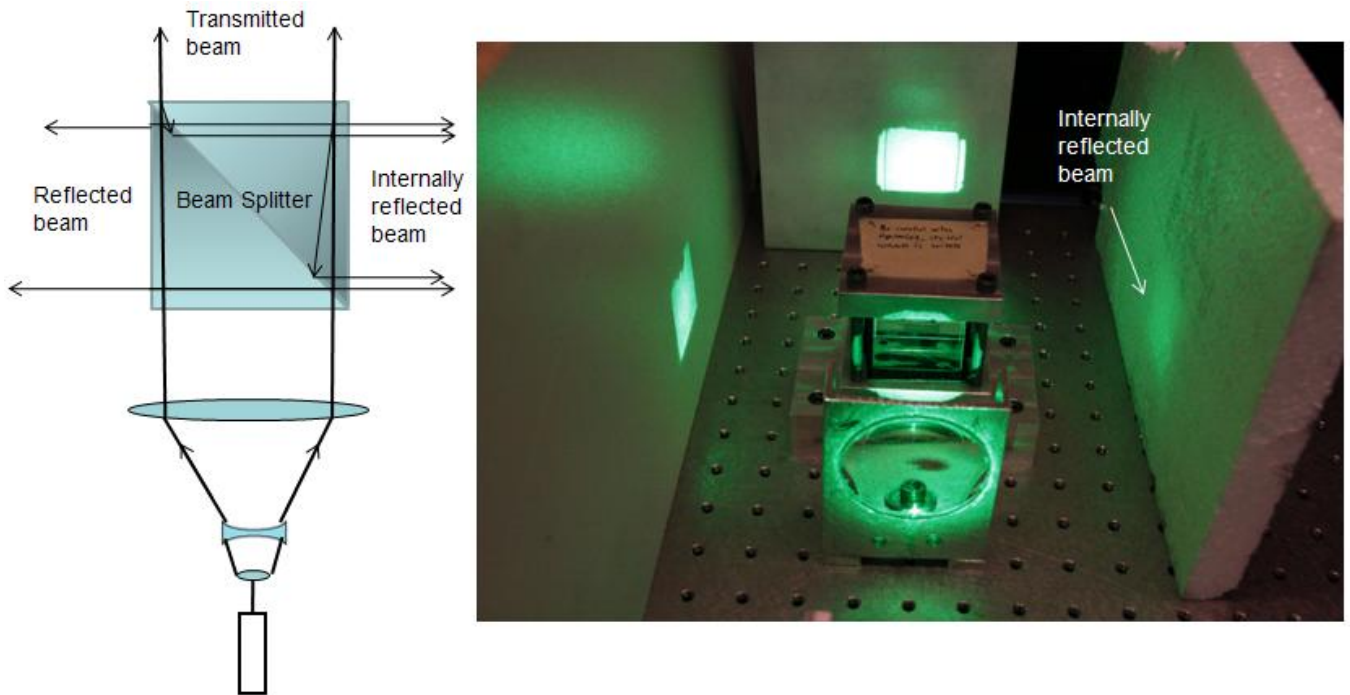


Figure 34: Beamsplitter Placement

3.4 Experiment Challenges and Solution

Any interferometer that can measure optical path length changes with nanometre resolution requires the stability of a number of environmental factors such as atmospheric conditions, vibrations and elastic deformations. The main challenge in measuring changes in the refractive index of the photoelastic material is that the refractive index of air, in which the light beam passes through changes along with changes in atmospheric conditions: Differential air temperature changes alter the refractive index of air and thus it can change the effective path difference between the two light paths of the interferometer. This effect can be observed by the drift in phase measurement values over time. To solve this problem, the optical equipments are enclosed in a closed cabinet to prevent air movement from affecting the phase stepping measurements. To prevent any vibrations from altering the optical path lengths, the

optical table rests on a granite table that provides vibration damping. Placements of air bearings under the optical table support structure provide additional damping.

Rigid-body motion is another source of unwanted measurement disturbance during phase stepping measurements. Given the sensitivity range of the measurement is the same as the wavelength of the illumination source or 532 nanometres, any movement of the optical components can result in drifts and offsets in the measurement. By observing the interference fringe pattern, it was found that the optical path length between the two arms of the interferometer arrangements changes by 20-50nm ($\lambda/25$ to $\lambda/10$) depending on the load placed on the specimen.

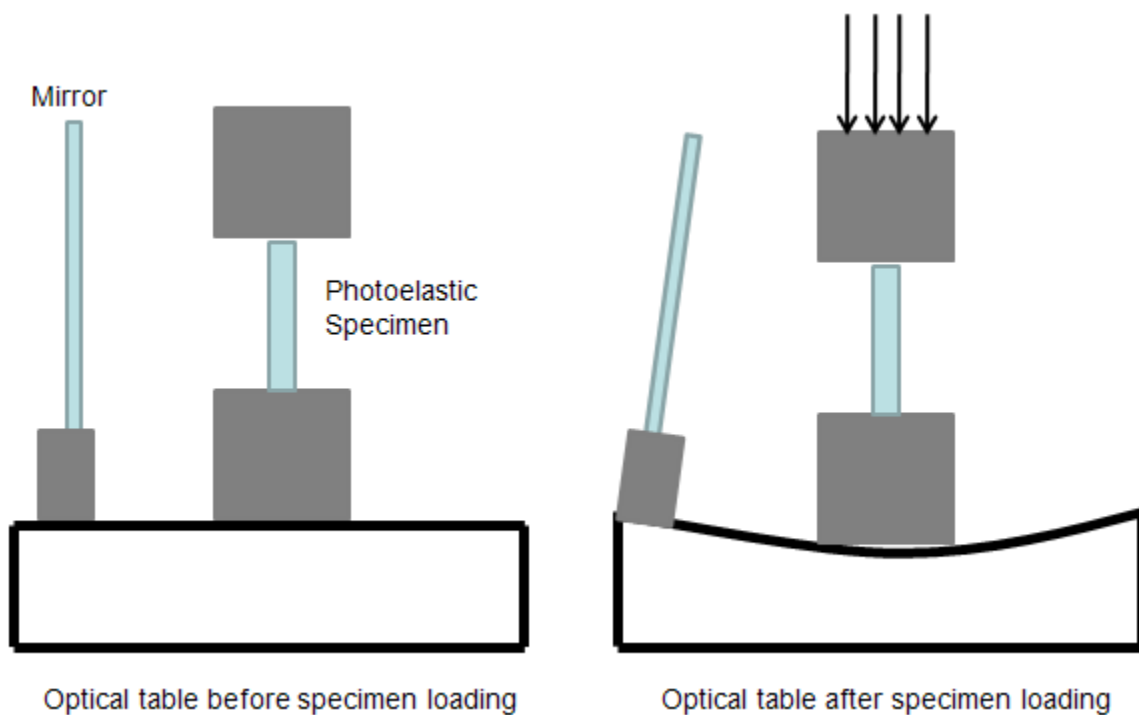


Figure 35: Static Deformation of Optical Table Due to Compression

As illustrated in figure 35, the optical table deforms as force is applied and the distances between the optical components are rearranged. This change is consistent and measurable in

the change in interference fringe pattern on the camera sensor. One can observe this effect by simply viewing the interference fringes through the camera and pushing the optical table with one finger. This deformation adds around 0.2 to 0.4 radians of offset drift to the phase stepping measurement. Two solutions are available to counter this effect; to use offset subtraction in the signal processing, or by preloading the optical table.

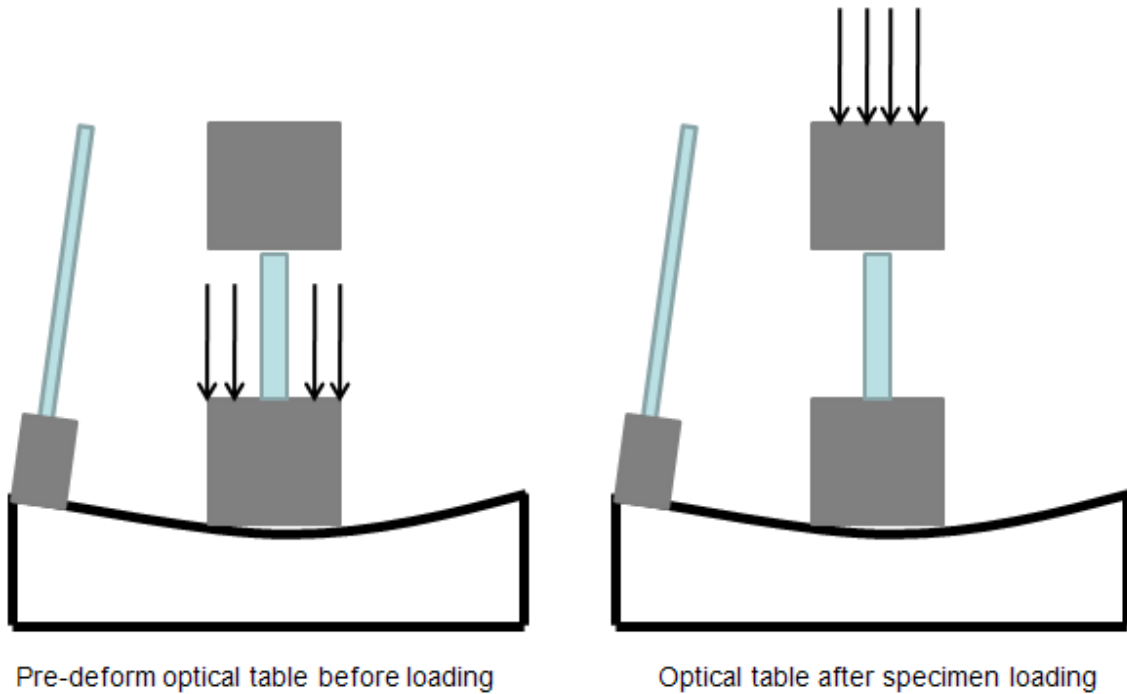


Figure 36: Deformation Compensation by Preloading

The rigid body offset is characterized to have a linear spatial gradient. Once modelled, the offset map can be subtracted from the measured phase map. This has been shown to be effective but time consuming. The second solution is to place the weight on the loading apparatus, without loading the specimen. This way the rigid body motion is eliminated when the loading is transferred through the specimen. This is illustrated in figure 36; the loading weight initially rests on loading structure without compressing the specimen and then

transferred onto the test specimen. This method is demonstrated to be as effective at treating rigid body deformation with manual drift compensation, without the additional signal processing procedure.

Chapter 4 – Experimental Validation

4.1 Experiment Overview

In this chapter, experimental validation of the tensor field photoelastic measurement of in-plane stresses is presented. The performance and accuracy of the method are evaluated by making measurements on photoelastic specimens of known stress distributions.

4.2 Photoelastic Test Specimen

The photoelastic material used for the tests is PMS-5 clear epoxy (Vishay, North Carolina). This material is manufactured to optical lens quality with highly transparent clear surfaces. The casting and machining processes used during manufacture are controlled to allow no visible residual stresses in the material.

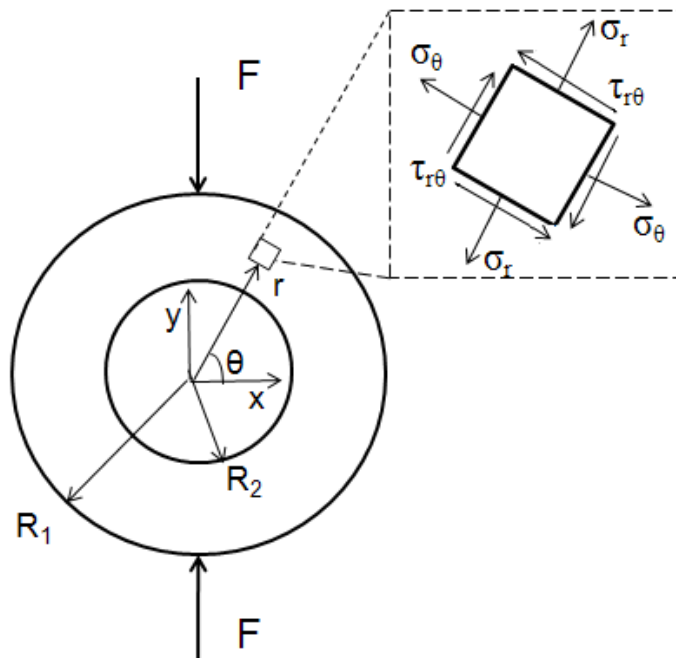


Figure 37: Circular Ring Specimen Under Compression

The material was machined into specimens in the shape of ring disks with an outer diameter 55mm, inner diameter 27.5mm and thickness 3mm. Figure 37 illustrates the ring geometry. A ring disk under diametral compression provides an interesting test specimen because the resulting stress distribution contains an easily visible mixture of all three components of in-plane stresses: normal stresses and shear stress. In addition, it contains some areas of high stress concentration. A closed-form analytical solution for the stress distribution within the ring is available [25] and provides a comparison with the measurements from the proposed photoelastic tensor field method. Where $\rho=R_2/R_1$.

$$\sigma_r = \frac{2P}{\pi b} \left[\frac{1}{2} - \frac{1}{2} \frac{\rho^2}{r^2} \left(\frac{1-r^2}{1-\rho^2} \right) - \frac{(1-r\cos\theta)(\cos\theta-r)^2}{(1+r^2-2r\cos\theta)^2} - \frac{(1+r\cos\theta)(\cos\theta+r)^2}{(1+r^2+2r\cos\theta)^2} \right. \\ \left. - \sum_{n=2}^{\infty} \{n(n-1)c_n r^{n-2} + (n+1)(n-2)d_n r^n + n(n+1)c'_n r^{-n-2} \right. \\ \left. + (n+2)(n-1)d'_n r^{-n} \} \cos n\theta \right] \quad (30)$$

$$\sigma_\theta = \frac{2P}{\pi b} \left[\frac{1}{2} - \frac{1}{2} \frac{\rho^2}{r^2} \left(\frac{1+r^2}{1-\rho^2} \right) - \frac{(1-r\cos\theta)\sin^2\theta}{(1+r^2-2r\cos\theta)^2} - \frac{(1+r\cos\theta)\sin^2\theta}{(1+r^2+2r\cos\theta)^2} \right. \\ \left. + \sum_{n=2}^{\infty} \{n(n-1)c_n r^{n-2} + (n+2)(n-1)d_n r^n + n(n+1)c'_n r^{-n-2} \right. \\ \left. + (n-2)(n-1)d'_n r^{-n} \} \cos n\theta \right] \quad (31)$$

$$\tau_{r\theta} = \frac{2P}{\pi b} \left[\frac{(1-r\cos\theta)(\cos\theta-r)\sin\theta}{(1+r^2-2r\cos\theta)^2} - \frac{(1+r\cos\theta)(\cos\theta+r)\sin\theta}{(1+r^2+2r\cos\theta)^2} \right. \\ \left. + \sum_{n=2}^{\infty} \{n(n-1)c_n r^{n-2} + (n+1)d_n r^n - (n+1)c'_n r^{-n-2} \right. \\ \left. - (n-1)d'_n r^{-n} \} \sin n\theta \right] \quad (32)$$

Where the coefficients are defined as:

$$c_n = \frac{1}{2(n-1)D} \left[n(\rho^2 - 1) + (\rho^{2n} - 1) - n^2 \left(\rho - \frac{1}{\rho} \right)^2 \right] \quad (33)$$

$$d_n = \frac{1}{2(n+1)D} \left[n^2 \left(\rho - \frac{1}{\rho} \right)^2 + n \left(\frac{1}{\rho^2} - 1 \right) - (\rho^{2n} - 1) \right] \quad (34)$$

$$c'_n = \frac{1}{2(n+1)D} [n(\rho^2 - 1) + (\rho^{2n} - 1)] \quad (35)$$

$$d'_n = \frac{1}{2(n-1)D} \left[n^2 \left(\rho - \frac{1}{\rho} \right)^2 - (\rho^{2n} - 1) \right] \quad (36)$$

$$D = \left[n^2 \left(\rho - \frac{1}{\rho} \right)^2 - \left(\rho^{2n} - \frac{1}{\rho^n} \right) \right] \quad (37)$$

The analytical stress distribution was converted from cylindrical to Cartesian coordinates using Mohr's circle axis transformation. A Matlab script was used to discretize the surface area of the ring disk into pixels of equal resolution to that of the measured data from the camera sensor. The analytical stress values for each pixel are then evaluated using the provided mathematical relationships. Forty terms were found to be more sufficient to evaluate accurately the convergence series within the analytical solutions in equations 30, 31 and 32.

Figure 38 shows the loading apparatus. It consists of a frame with guided rails and a steel mass placed on top. The guided rails rest on the specimen to prevent sideways motion. The loading procedure is explained in section 3.4. The specimen is loaded and unloaded 4 times during the 4 sets of phase measurements. Any rigid body motion of the specimen during the testing procedure will cause disturbances in the phase measurements.

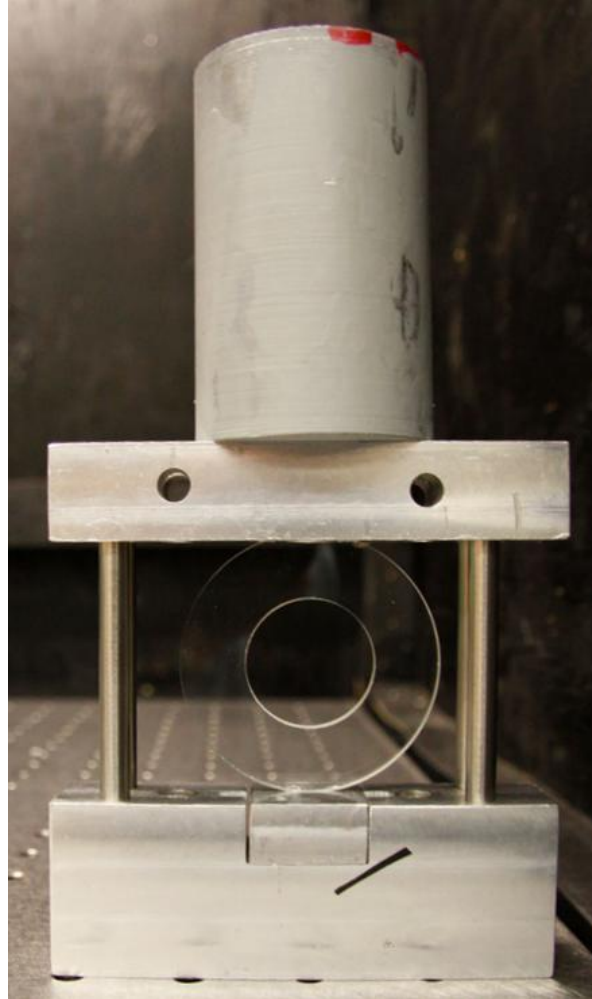


Figure 38: Photograph of Test Specimen and Loading Apparatus

4.3 Polarized Phase Measurement of Birefringence

As described in section 2.5, the three in-plane stress components can be determined from at least three sets of phase stepped measurements. For greater computational stability and convenience, four sets of stepped measurements are used here, as detailed in section 3.2.3. The four sets of phase-shifted measurements are taken with the polarizing filters oriented at 45° intervals. Two attenuators are adjusted for each polarization angle, to balance the beam intensities and to avoid saturation of the camera sensor. Figure 39 displays the four sets of

phase measurements as computed fringes. The white areas of the plot indicate phase changes of even multiples of π and the black areas odd multiples of π . The phase values within the region around the outside of the specimen are averaged and subtracted from the phase values within the entire image. This is done to compensate for any drift in the phase measurement due to air temperature variations. The measured phase is “wrapped”, i.e., specified within a 2π cycle such as in figure 39. The Goldstein algorithm [24] was used to unwrap the phase results into a continuous map.

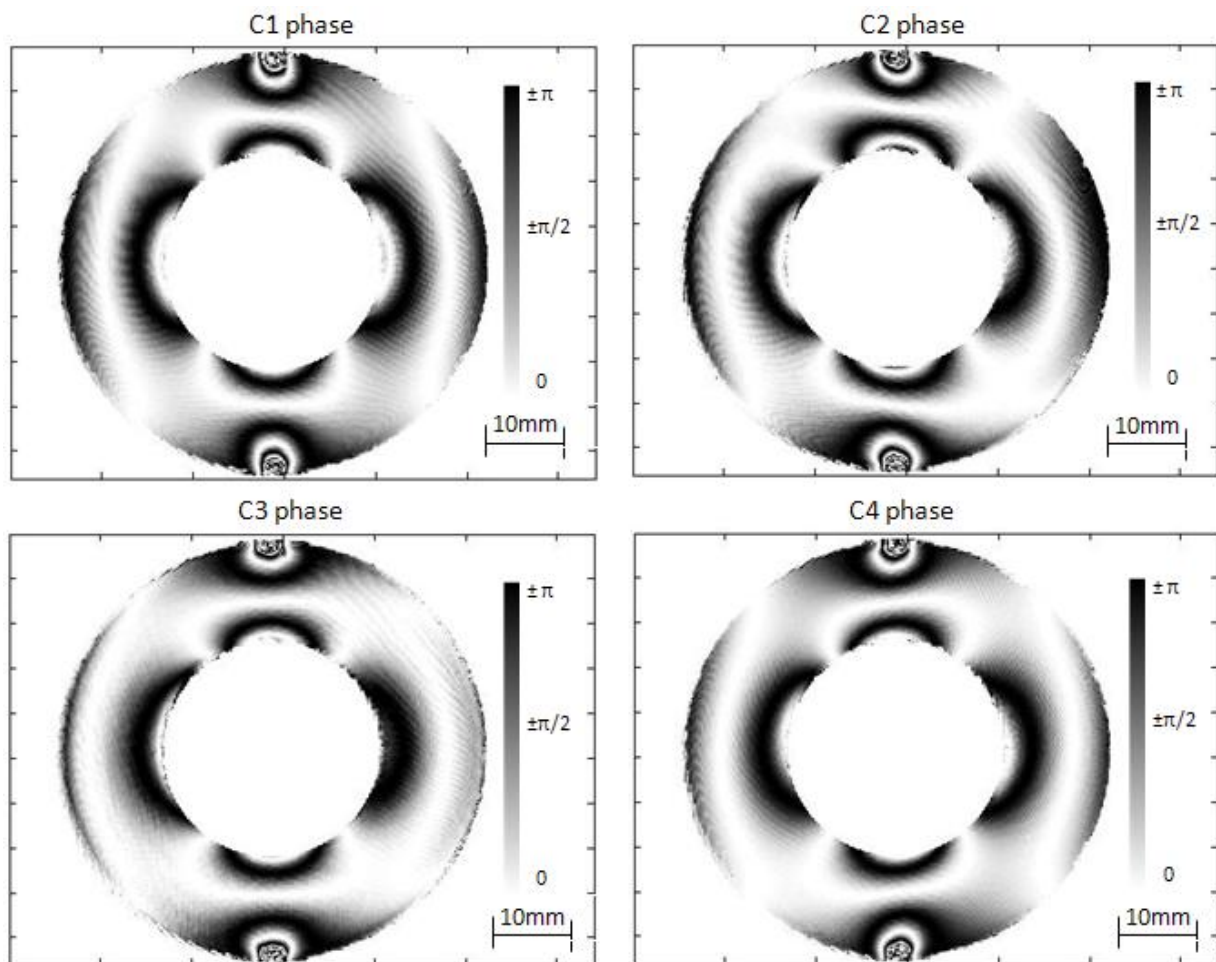


Figure 39: Polarized Phase Measurements

The tightly packed fringes on the top and bottom of each phase map shows high stress concentrations at the points of contact, while the more widely spaced fringes in other areas show more gradually varying stresses. The C1 and C3 measurements should be symmetrical because of the symmetrical position of the polarizing filter; horizontal for C1 and vertical for C3. The C2 and C4 measurements have a diagonal bias because they are illuminated with diagonal polarizations.

4.4 Calculation of Principal Transmission Factors

After unwrapping the computed phase maps illustrated in figure 39, a numerical smoothing filter is applied to reduce the image noise content. The complex transmission factors that characterize the birefringence (C1, C2, C3 and C4) are assigned unity amplitude because photoelastic birefringence causes phase changes only without attenuation. The principal transmission factors u and v are calculated according to equation 21 in section 2.3. The square root term $\sqrt{q^2 + t^2}$ needs to be examined in order to determine its correct sign. A phase map corresponding to this term is first unwrapped, if it has an even multiple of π at a given pixel then the square root term locally is positive, if an odd multiple it is negative. The principal transmission factors can then be determined explicitly. The principal angle is estimated by computing the inverse tangent of the numerically larger of the real or imaginary components of the transmission factors t and q . This process occasionally gives $\pi/2$ jumps in the principal phase direction whenever the relative sizes of the principal stresses interchange. This artifact is easily corrected by unwrapping of the principal angle (θ) map with $\pi/2$ unwrapping. Figure 40 shows the two principal phase shifts (phase maps of u and v), and the principal angle plot, with the x axis as its reference and counter clockwise rotation defined as positive.

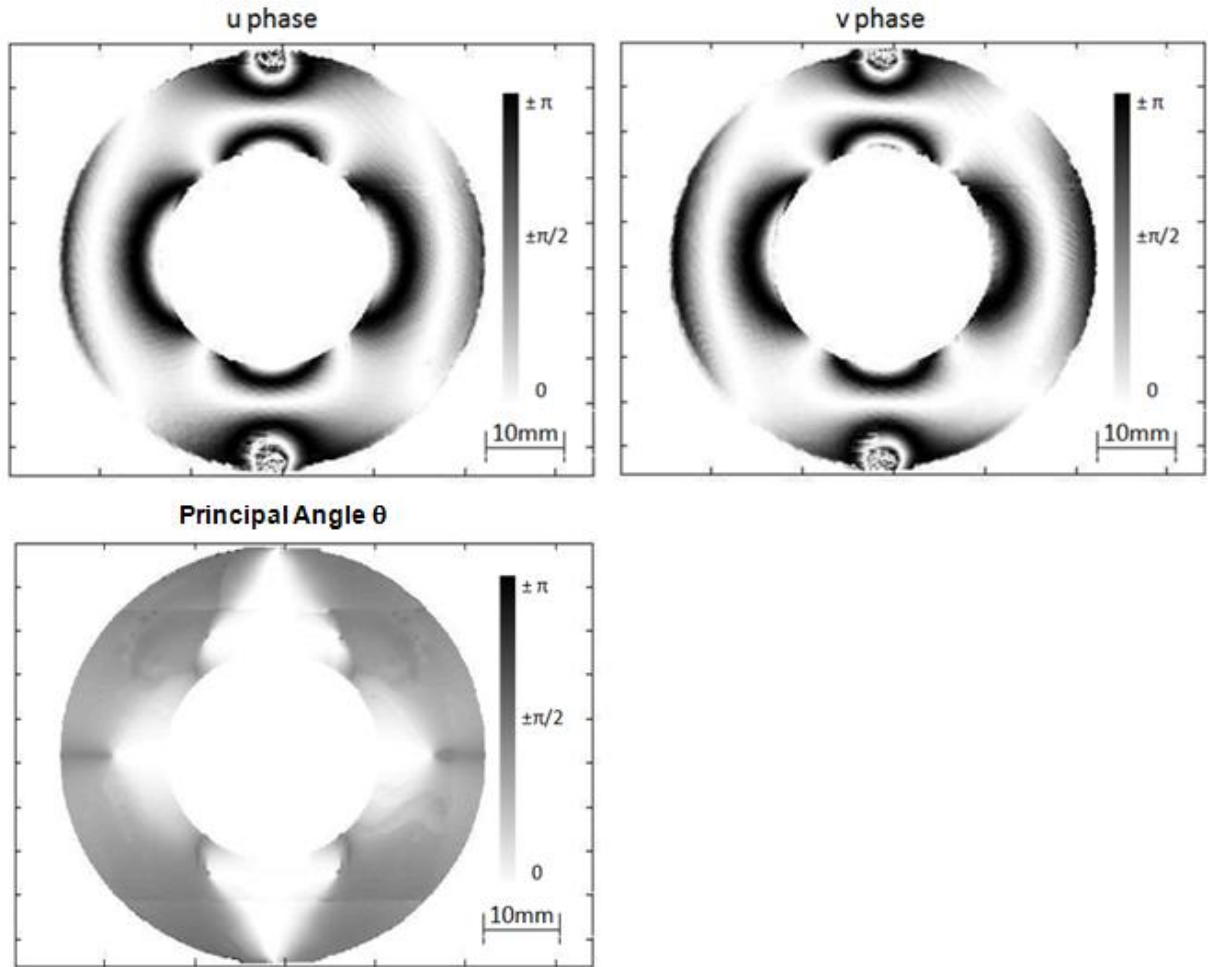


Figure 40: Calculated Principal Components of Birefringence

4.5 Stress Optical Coefficient Evaluation

The stress optical coefficients of PMS-5 are experimentally determined by comparing the phase maps of the calculated principal transmission factors u and v with the analytical principal stresses. The relationship is expressed in equation set 12 of section 2.3. For the PMS-5 material, the stress-optical coefficients A and B were found to be $A=100\times 10^{-12}$ rad/Pa and $B=130\times 10^{-12}$ rad/Pa.

The stress coefficient evaluation procedure involves comparing the polarized phase maps shown in section 4.3 with that of the analytical solution. The stresses in the analytical solution is converted into optical phase values through the stress optical relationship. From there, forward Mohr's circle transformation is applied to obtain the theoretical polarized phase maps. The two phase maps can then be compared to determine the correct stress optical coefficients. In the event that the phases do not match, the values and A and B can be adjusted such that the analytical phase matches with the measured phase. Figure 41 below shows a close match between the measured C3 phase and that of the analytical solution.

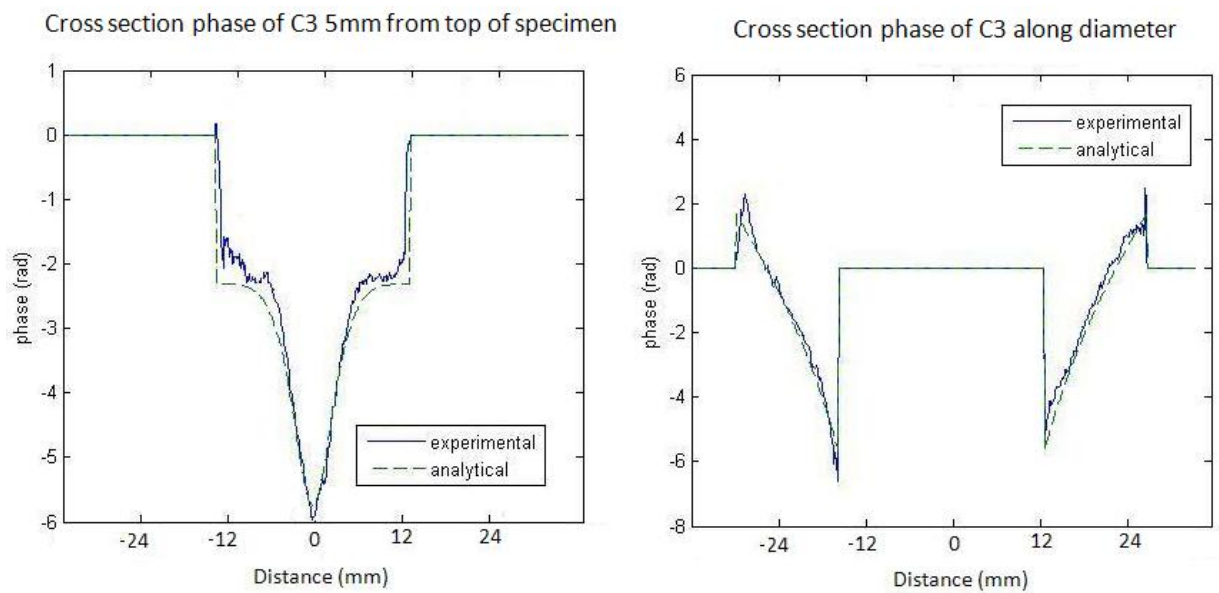


Figure 41: Cross Section Phase Comparison of C3

4.6 Stress Distribution Comparison

The principal stresses of the specimen are calculated according to equation set 12 of section 2.3. Mohr's circle transformation is used to present the three in-plane stress components in

Cartesian representation. For more direct visual interpretation, Figure 42 presents the stress distributions as “stress fringe” plots, with each fringe corresponding to an interval of 200 kPa. The fringes in these plots indicate contours of stress at 200 kpa intervals. The calculated stress distributions from measured data are presented on the left, while the analytical stress distributions are presented on the right. Overall, the stress components extracted from measured data closely correspond to the analytical solution, with some deviations in the areas of stress concentration at the contact points. By examining a horizontal cross section of the circular ring located a half the distance between the top and middle, the stress values of the experimental solution with the analytical, as shown in figure 43. The horizontal scales shows the distance away from the edge of the image. The center portion of the plots where the stress values are 0 represent the hollow center of the ring. The numerical cross section comparison shows a 10% maximum error.

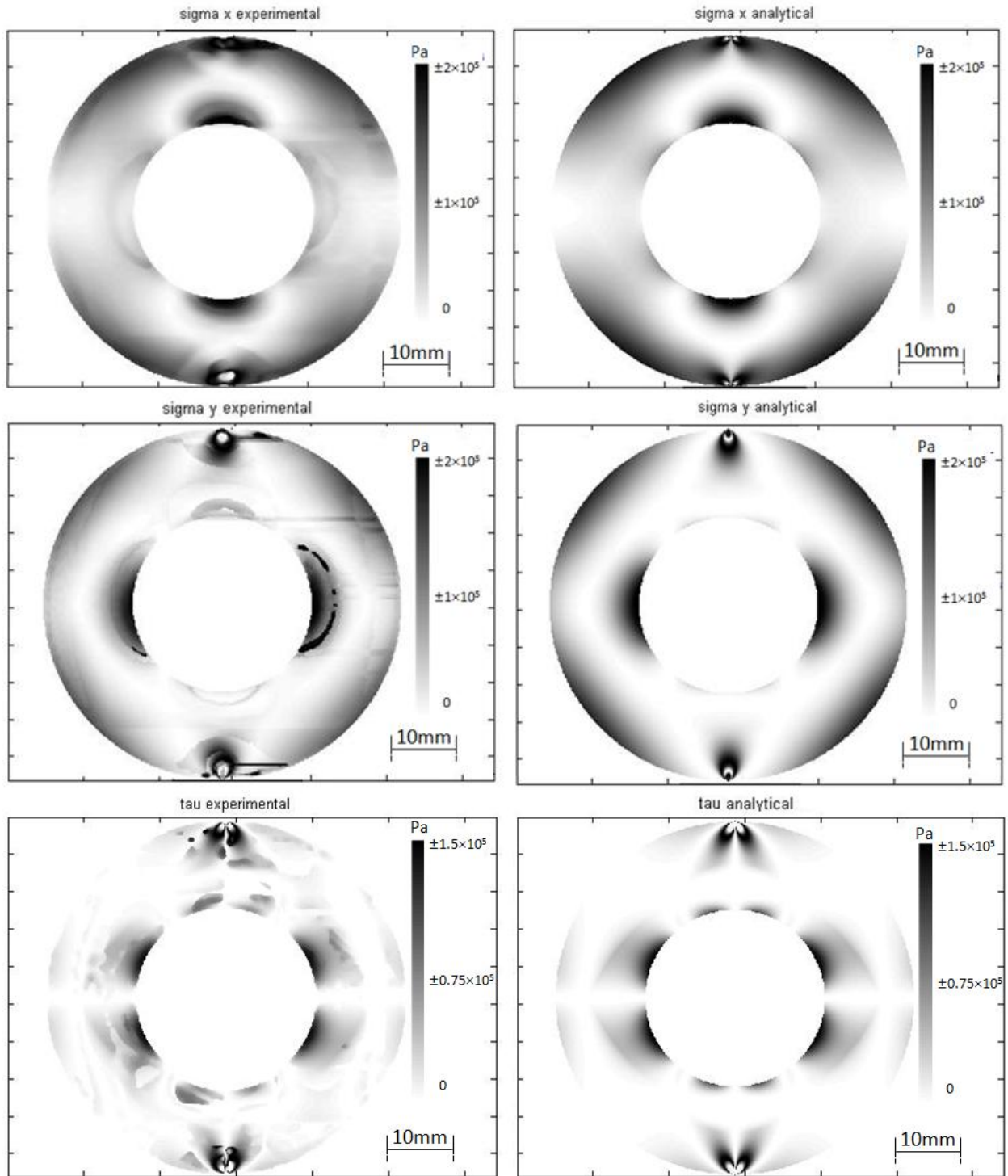


Figure 42: In-Plane Stress Distribution Comparison

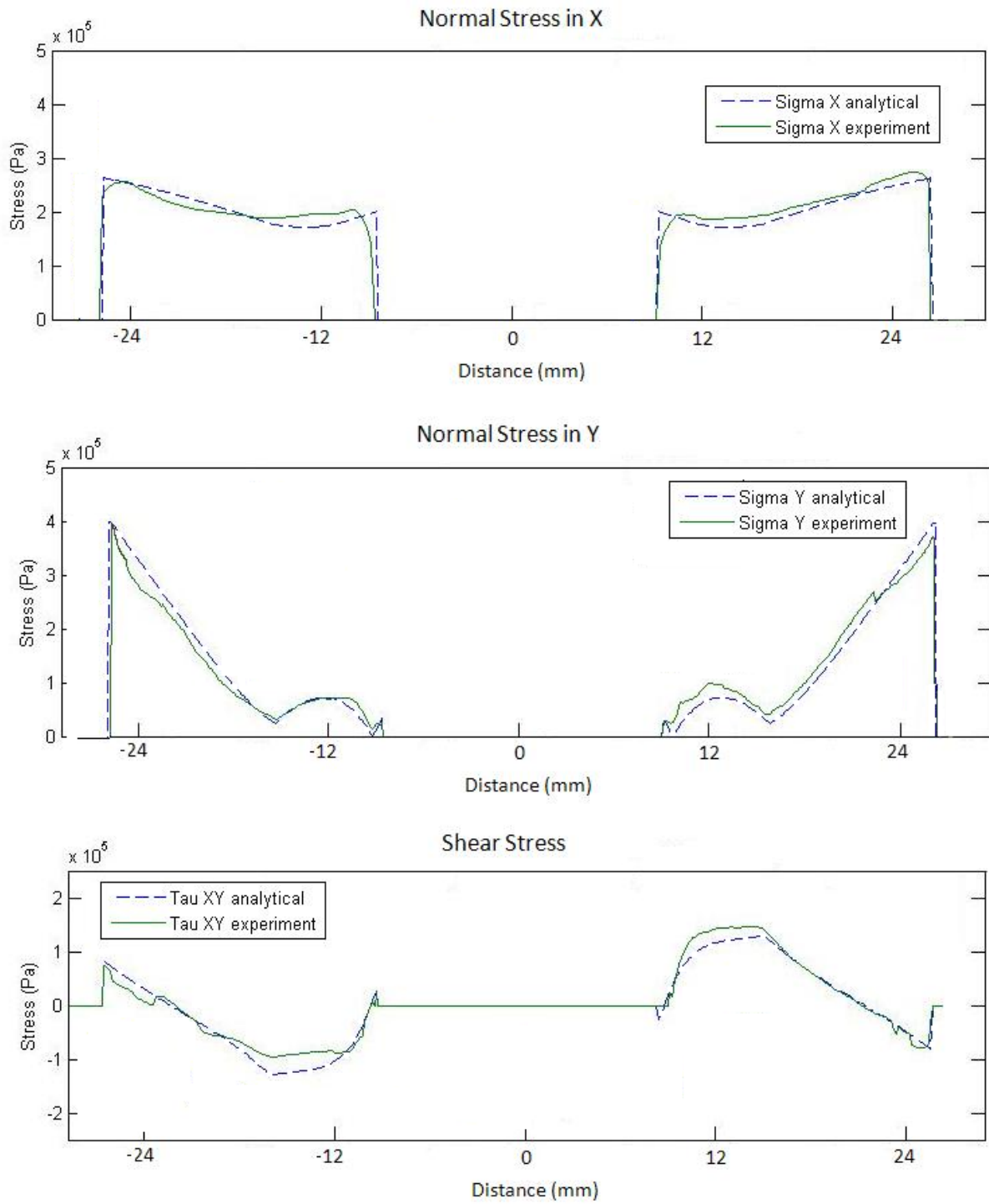


Figure 43: Measured and Analytical Stress Profiles Along a Horizontal Line a Quarter Diameter Below the Upper Contact Point.

Figure 43 shows a comparison of profiles of the three Cartesian stress components along an example horizontal line a quarter of the outside diameter below the upper contact point. It can be seen that all three Cartesian stress components are evaluated separately and realistically. The calculation is automatic and requires no human guidance. This individual evaluation of all three stress components represents a significant advance over the conventional photoelastic method where at best two stress components can be determined.

Chapter 5 – Discussions

5.1 Comparison with Classical Photoelastic Method

From the measurements of a known stress field presented in the last chapter, the tensor field photoelastic method of measuring in-plane stresses has been shown to be effective. The proposed method measures the absolute variation in optical phase, as opposed to the relative phase change in the classical photoelastic method. A typical optical arrangement for classical photoelastic measurement is illustrated below.

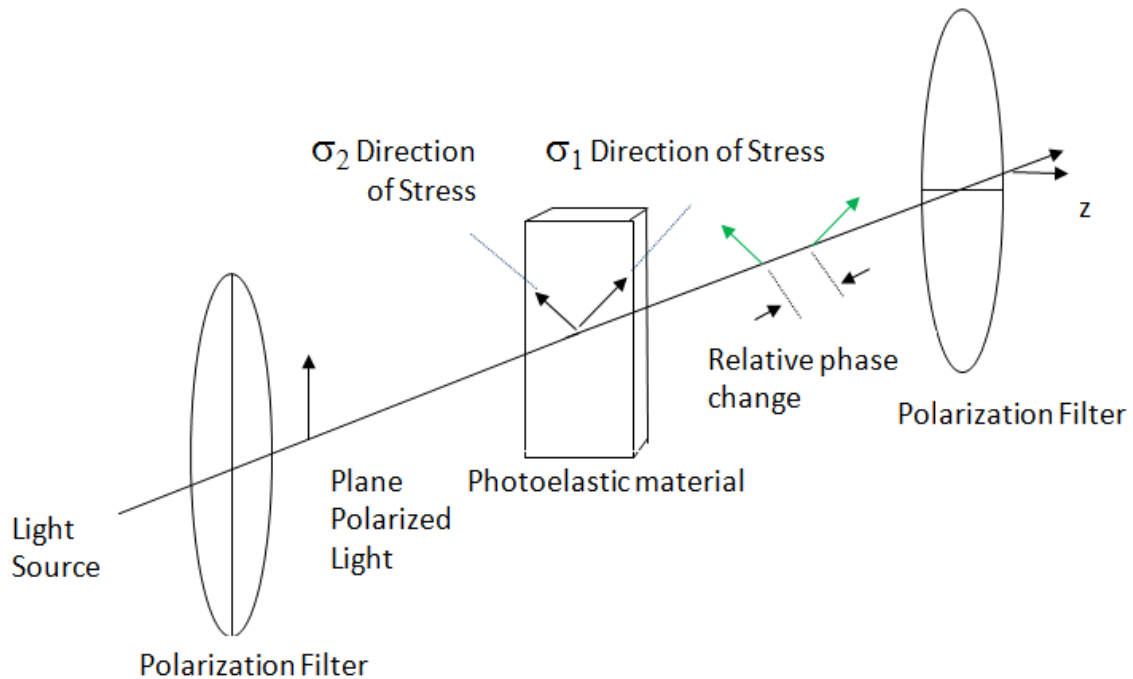


Figure 44: Classical Photoelasticity Optical Arrangement

The first polarization filter (left) polarizes light before passing through the photoelastic specimen. The stresses in the specimen cause each polarization component of light in the directions of the two principal stresses to change. This causes relative phase change between

the two polarization components, and in turn depolarizes the polarized light. The second polarization filter oriented orthogonal to the first filters out the vertically polarized components, while allowing the depolarized component to pass through. This optical arrangement produces stress fringes that are functions of the relative phase changes and the principal direction. [10] The measurement of the relative phase changes alters the stress optical relationship discussed in equations 12 of section 2.3. The classical photoelastic stress optical relationship expressed below.

$$\begin{aligned}\phi'_1 - \phi'_2 &= \frac{2\pi}{\lambda} [A (\sigma_1 - \sigma_2) + B (\sigma_2 - \sigma_1)]d \\ \phi'_1 - \phi'_2 &= \frac{2\pi}{\lambda} [(A - B) (\sigma_1 - \sigma_2)]d\end{aligned}\tag{38}$$

The test material used in Chapter 4 has stress coefficient values of $A=100 \times 10^{-12} \text{m}^2/\text{N}$ and $B=130 \times 10^{-12} \text{m}^2/\text{N}$. The difference of these values is about one third the size of the individual values. Consequently, the sensitivity of the proposed method is about three times greater than the classical method.

The two photoelastic measurement methods are compared by testing the same specimen presented in chapter 4 with the classical method. A polariscope is used, where the two polarization filters are placed orthogonal to each other, as illustrated in figure 44. The ring specimen is loaded with the same loading apparatus and performed under the same loading conditions.. The difference in sensitivity is between the two methods is quite clear; the fringes produced by the classical method are visually difficult to distinguish, whereas the computed fringes in figure 39 very highly visible. The benefit of increased sensitivity of the tensor method allows measurements using lower loads. This reduces the deformation of specimens and thus reduces the effects of geometrical distortions.

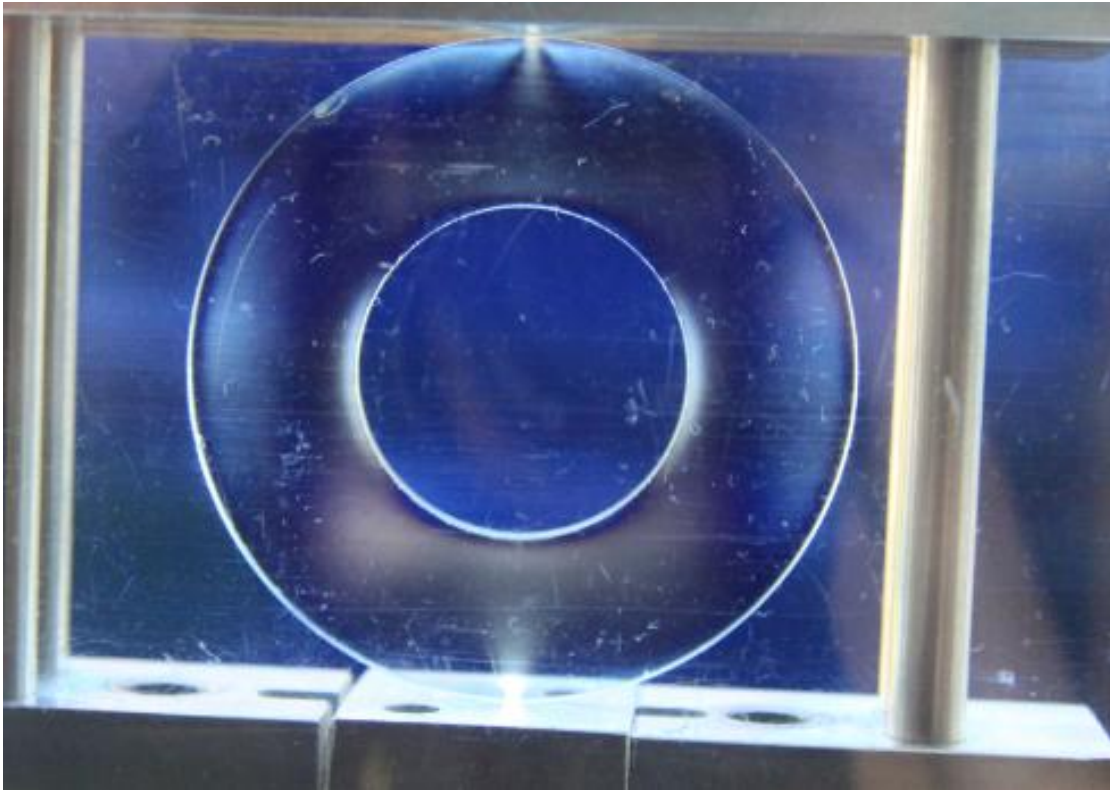


Figure 45: Classical Photoelastic Fringe Observation

5.2 Improvements to Current Measurement Method

The main drawback to the demonstrated measurement method is its user inconvenience compared to the simpler classical photoelastic method. Currently the measurement procedure consists loading and unloading the specimen four times to produce the four sets of polarized phase measurements. Theoretically it is possible to load the specimen only once and take the sets of polarized phase measurements while rotating the polarization filter. It is discovered that this measurement procedure is not practical with the current equipment due to the manual polarization adjustment as elaborated in section 3.2.4. The rotation of the polarization filter produces noise to the phase measurements. As demonstrated by a test shown in figure 46,

during piezo-actuated phase measurements, the polarization filter located in front of the specimen is rotated incrementally (1° intervals) clockwise and then rotated back to its original position. The top left image shows a drift compensated phase fringe plot with no action. The top right image shows the polarization filter rotated by 1° . Roughness features of the polarizer lens appear, as their position changes. Greater rotation of the polarizer shows the same features followed by bulk rigid body motion, as shown on the bottom left of the figure.

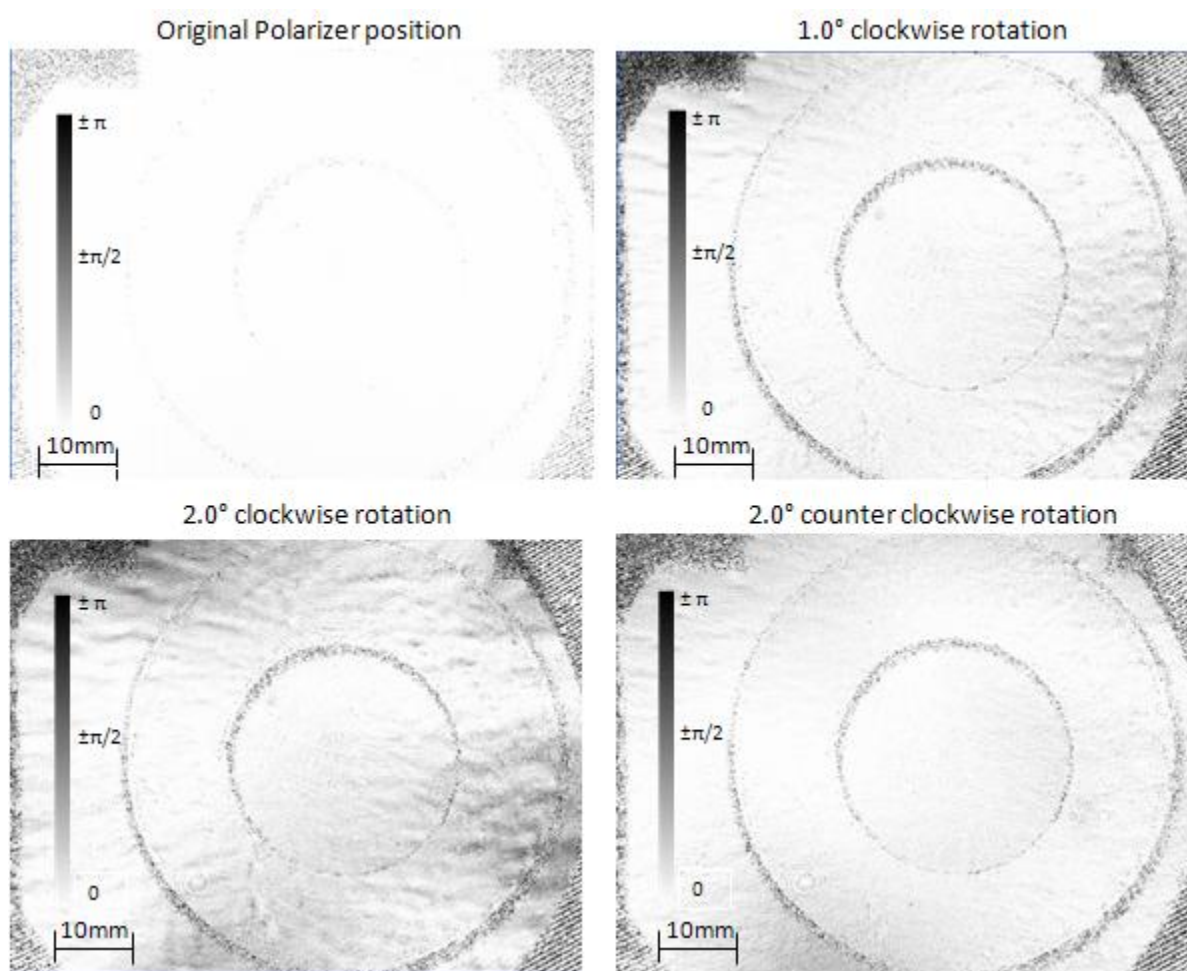


Figure 46: Phase Disturbance From Polarizer Movement

When the polarizer lens is rotated back to its original position as shown on the bottom right image, some roughness and bulk rigid body motion features remain. This is likely due to the

lack of mechanical precision in the mechanical mounts. The manual adjustment only allows 0.5° accuracy in rotation. Even though the roughness of the lens is within a quarter wavelength, these values are too large for phase calculations. For the application of loading the specimen once, the polarization filter needs to travel 45° intervals and travel back to its exact locations, without causing disturbances in the phase measurements. The recommended solution to the measurement equipment is to automate the polarization filter. Precision motion control of polarization rotation is necessary, because distortions can be eliminated by positioning the polarization filter back to its position when the initial phase shift measurements are taken.

5.3 Future Work and Applications

This research has demonstrated the ability to measure all three components of in-plane stresses using tensor field photoelasticity. So far the application is limited to flat plate photoelastic materials. The use of a Michelson type interferometer in the optical arrangement provides the possibility of applying this measurement technique to reflection photoelasticity. Reflection photoelasticity is a well-established field, where the surface stress/strain information can be measured by applying thin coating of photoelastic coating to a solid surface of interest [5][8]. The arrangement is illustrated below in figure 47. The photoelastic material has a lower Young's modulus than the material attached.

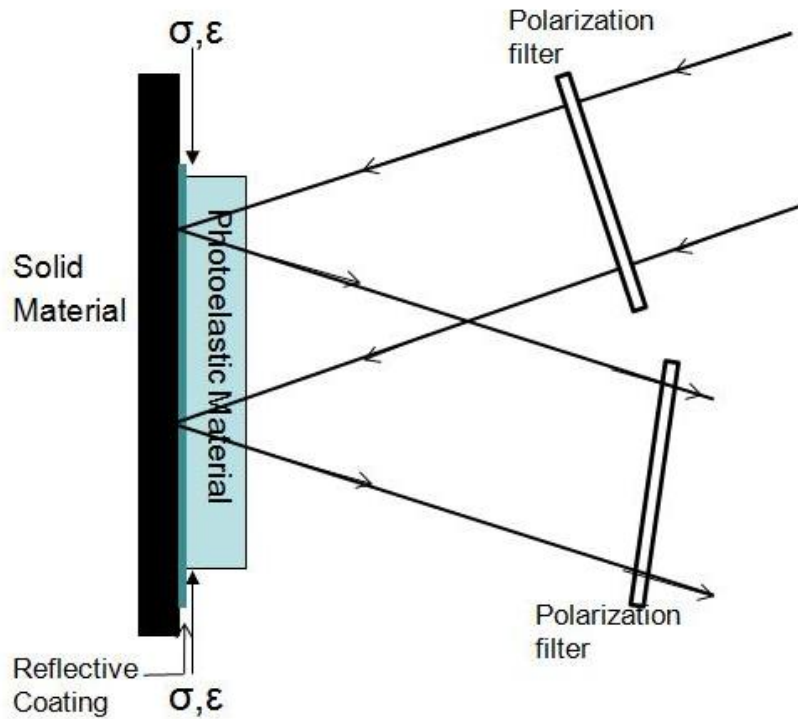


Figure 47: Surface Strain Measurement Using Reflection Photoelasticity

The result is that during deformation, the strain of the material is equal to the strain of the photoelastic coating. Since both materials are isotropic and linearly elastic, the measured stresses in the photoelastic coating mathematically translate to the strain deformation of the solid material.

Currently the measurement technique used in reflection photoelasticity uses the same optical arrangement as classical photoelasticity [10]: where a pair of polarization filters is used to construct a polariscope. The same optical arrangement signifies that reflection photoelasticity has the same limitations as classical photoelasticity: that it cannot measure all in-plane stresses/strains. As illustrated below in figure 48, the Michelson interferometer arrangement presented in chapter 3 provides the possibility of applying the tensor field

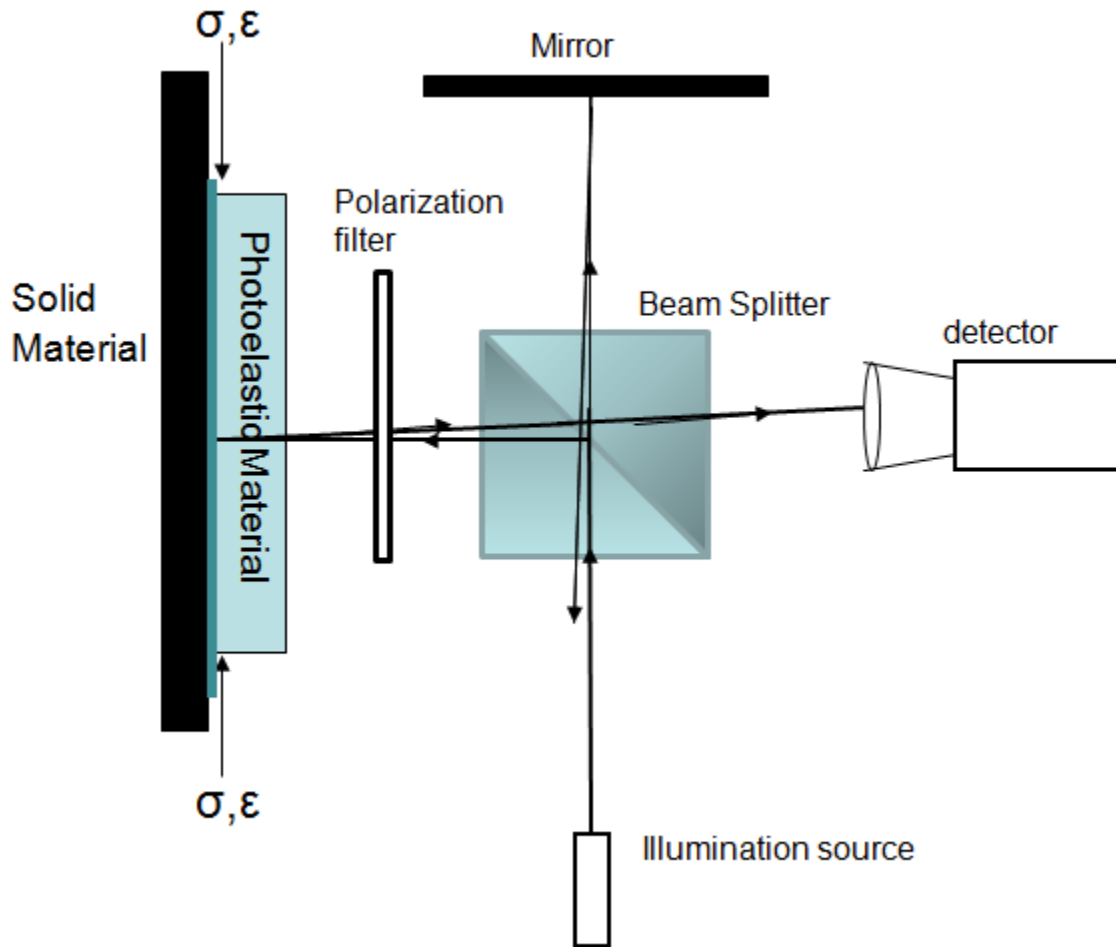


Figure 48: Applying Tensor Field Measurement to Reflection Photoelasticity

measurement technique to reflection photoelasticity measurements. The advantage of this arrangement is to provide full field experimental data on all 3 components of stress/strain. An advantage of this optical arrangement is the perpendicular ray angles of both illumination beam and reflected beam, compared to the oblique angle in the classical reflective method. This reduces any measurement distortions caused by the oblique viewing angle.

A significant challenge exists in the proposed method; the rigid body motion caused during the deformation distorts the phase measurements. This issue does not exist in the polariscope arrangement due to the relative phase retardation nature of the measurement, i.e.

the difference in optical path length between the polarization components are not affected by the movement of the photoelastic material, whereas the absolute variation in optical path length in the Michelson interferometer are affected by three factors: photoelastic birefringence, rigid body motion and change in the refractive index of air (drifts). As illustrated in figure 48, the reflective coating between the photoelastic coating and the solid materials acts as a mirror for the interferometer. The reflective coating changes location as the solid material deforms, thus causing rigid body fringes in the phase measurements. A solution is thus needed to identify and separate the rigid body motion from the phase measurements.

Chapter 6 – Conclusions

6.1 Research Summary and Contributions

A new photoelastic stress measurement method is described and demonstrated for full-field evaluation of all three in-plane stress components within a two-dimensional photoelastic material. The measurement method is based on the observation that the complex transmission factors that describe optical phase changes due to stress-induced birefringence have a second order tensor character, similar to that of other tensor quantities such as stress and strain. The same transformation equations and Mohr's circle construction are applied to the rotation of optical axis. The birefringence tensor field is characterized by two principal transmission factors and an axis orientation angle much like other second order tensor quantities such as mechanical stress. A Michelson type interferometer is used to conduct phase shifting measurements to identify the change in absolute variation in optical phase in the photoelastic test specimen. The phase changes are caused by the applied stress on the specimen. A plane polarization filter is used to isolate specific transmission factors. The measurement procedure consists of taking four sets of phase measurements with the polarization filter alignments at 45-degree rotational increments. Complex transmission factors characterize the optical attenuation and phase changes. A complex Mohr's circle is constructed from the four measured transmission factors. The principal transmission factors and principal axis orientation are then extracted, which in turn provide the principal stresses and corresponding angles. The effectiveness of this technique is demonstrated by measuring photoelastic specimens containing known stress distributions and comparing the experimental results with the theoretical solutions.

The Michelson type interferometer demonstrated here has proven effective at measuring absolute variation of optical phase in photoelastic birefringence. The two advantages of this optical configuration over the existing Mach-Zehnder type interferometers are the double birefringence sensitivity and the enlarged field of view. By allowing light to pass through the photoelastic specimen twice, the stress optical sensitivity is doubled. The two-stage beam expansion optical arrangement allows the use of specimens of larger size than the optical components conventionally used in an interferometer. The challenges faced in conducting measurements, such as air turbulence disturbance and static deformation during loading, are resolved through the use of drift compensation in the phase measurements and preloading the loading apparatus as explained in section 3.2 and 3.3. The alignment process of this optical arrangement is slightly more difficult than when using a Mach-Zehnder type interferometer: This is because the two-stage beam expansion feature requires the expanded laser beam to be perfectly parallel before entering the second beam expander. A divergence of the beam creates double edges around the specimen.

6.2 Comparison with other in-plane stress measurement methods

Full field stress measurement methods provide continuous data throughout an area of interest, not available to selected point-wise sampling in discrete measurements. The demonstrated measurement method allows all three components of in-plane stresses to be directly evaluated using a single test arrangement, as opposed to multiple test equipments in hybrid methods where multiple measurement techniques are combined.

In comparison with the classical photoelastic measurement method, the demonstrated method is somewhat less convenient because of the use of a more delicate optical arrangement.

The demonstrated method uses a Michelson type interferometer to characterize the birefringence induced by the in-plane stresses that is susceptible to environmental disturbances such as air pressure drifts and rigid body motion, whereas classical photoelasticity utilizes a polariscope that is immune to these environmental factors. The main drawback of classical photoelastic measurement is that it cannot identify all three components of in-plane stresses. Another drawback is the relative phase retardation nature of the polariscope, only the difference in optical phase between the polarization components in the directions of the principal stresses is examined. The stress optical relationship thus becomes a function of the difference between two stress optical coefficients. In the cases where the two stress optical coefficients are close to equal values, the sensitivity is greatly diminished.

In comparison with indirect methods of measuring all three components of in-plane stresses, such as combining classical photoelastic measurement with interferometric measurements, the proposed method avoids the need for stress separation and thus reduces the number of measurements needed. The two methods are comparable, since both use similar optical interferometer equipments. The key difference is that the discussed method relies on interpreting intensity measurements to solve non-linear relationships of the stress components, and the presented method directly measures optical phase and treats the birefringence as a tensor quality, in which the optical stress relationships are linear. As Nisida and Saito noted in 1964, both classical and interferometric intensity measurements contain non-linear relationship between the stress components [11] and this was addressed by Yoneyama, Morimoto, and Kawamura in 2005 [13]. Their measurement method consists of taking a number of intensity measurements by rotating two polarization filters and a quarter wave plate. The tensor field measurement method demonstrated here simplifies the number of

measurements needed by directly measuring optical phase changes instead of optical intensity, where both the tensor field transformation used and stress optical relationship are linear. This reduces polarization control down to one polarizing filter and the number of measurements required to four sets of automated phase shifted measurements.

References

- [1] Beer, F.P., Johnston, E.R. and DeWolf, J.D. 1992. "Mechanics of Materials." McGraw-Hill Professional. New York.
- [2] Peng, L, Wang J and Zhu Q., 1995, "Methods with high accuracy for finite element probability computing", Journal of Computational and Applied Mathematics no. 59, p. 181-189.
- [3] Babuska, I. Banerjee, U. and Osborn, J.E., 2004, "Generalized Finite Element Methods: Main Ideas, Results, and Perspective". International Journal of Computational Methods no.1, p. 67–103.
- [4] Groshong, R.H., Teufel, L.W. and Gasteiger, C., 1984, "Precision and accuracy of the calcite strain-gage technique", GeoScience Work Bulletin, v. 95; no. 3; p. 357-363
- [5] Sharpe, J. and William, N. 2007, "Springer Handbook of Experimental Solid Mechanics." Springer. New York.
- [6] Lord, H.W. and Shulman, Y., 1967, "A generalized dynamical theory of thermoelasticity" Journal of the Mechanics and Physics of Solids v. 15, no. 5, p. 299-309
- [7] Bornert, F.M. and Doumalin, B.P., 2009, "Assessment of Digital Image Correlation measurement errors: methodology and results." Journal of Experimental Mechanics v. 49, no. 3 p. 353-370
- [8] Dally, J.W. and Riley, W.F. 1991. "Experimental Stress Analysis, 3rd ed." McGraw-Hill, New York.

- [9] Ainola, L. and Aben, H. 2004. "On the optical theory of photoelastic tomography." Optical Society of America. v..21, no.6, p.1093
- [10] Burgur, C.P. 1993. "Photoelasticity Handbook on Experimental Mechanics." Kobayashi. VCH, New York. pp. 165-266.
- [11] Nisida, M. and Saito, H. 1964, A new Interferometric method of two-dimensional stress analysis. Experimental Mechanics, v 4, n 12, p 366-376,
- [12] Theocaris, P. S. and Gdoutos, An interferometric method for direct evaluation of principal stresses in plane-stress fields. J. Phys. D: Appl Phys., Vol, 7, 1974. Britain.
- [13] Yoneyama, S., Morimoto, Y., and Kawamura, M., 2005, "Two-dimensional stress separation using phase-stepping interferometric photoelasticity Measurement." Science and Technology, v 16, n 6, p 1329-1334.
- [14] Boresi, A.P., Schmidt, R.J., and Sidebottam, O.M., 1993, "Advanced Mechanics of Materials, Wiley", New York.
- [15] Schajer, G.S. and Orhan, F.B., 2005, "Microwave Non-Destructive Testing of Wood and Similar Orthotropic Materials." Subsurface Sensing Technologies and Applications, v. 6, no. 4, p. 293-31.
- [16] Hariharan, P. 1985, Optical Interferometry, Academic Press. Sydney, Australia
- [17] Timoshenko, S.P. and Goodier, J.N., 1970. "Theory of Elasticity Third ed." McGraw-Hill International Editions. USA
- [18] Theocaris, P. S. 1973. Dependence of stress-optical coefficients on the mechanical and optical properties of polymers. J. Strain Analysis. Vol.8, No.4, pp. 267

- [19] Schajer, G. S. 1988, Measurement of non-uniform residual stresses using the hole-drilling method. Part I: Stress calculation procedures: J. Engineering Materials and Technology, v.110, No.4, pp.338–343.
- [20] Lipson, S.G., Lipson, H. and Tannhauser. D.S.,1995, Optical Physics 3rd Edition, Cambridge University Press, UK
- [21] Sirohi RS, Chau FS. “Optical Methods of Measurement: Wholefield Techniques”. Marcel Dekker, Inc. New York, NY. 1999.
- [22] Francon, M., 1966, Optical Interferometry, Academic Press. New York
- [23] Brown, B.B., 1945, Optical Instruments, Chemical Publishing Co. Inc. Brooklyn, N.Y
- [24] Kadono H, Takei H. “A Noise-immune Method of Phase Unwrapping in Speckle Interferometry”. Optics and Lasers in Engineering. Vol. 26, pp. 151-164, 1997.
- [25] Chianese, R.B., Erdlac, R.J, The General Solution to the Distribution of Stresses in a Circular Ring Compressed by Two Forces Acting Along a Diameter. J. Mech. Appl. Math., v.41, Pt. 2, 1998. Oxford UK
- [26] Yu, F.T.S and Khoo I.C., 1990, Principles of Optical Engineering, John Wiley & Sons. Toronto